

# The cosmic evolution of the spatially-resolved star formation rate and stellar mass of the CALIFA survey

R. López Fernández<sup>1</sup>, R. M. González Delgado<sup>1</sup>, E. Pérez<sup>1</sup>, R. García-Benito<sup>1</sup>, R. Cid Fernandes<sup>2</sup>, W. Schoenell<sup>3</sup>, S. F. Sánchez<sup>4</sup>, A. Gallazzi<sup>5</sup>, P. Sánchez-Blázquez<sup>6</sup>, N. Vale Asari<sup>2</sup>, C. J. Walcher<sup>7</sup>

<sup>1</sup> Instituto de Astrofísica de Andalucía (CSIC), P.O. Box 3004, 18080 Granada, Spain. (e-mail: rosa@iaa.es)

<sup>2</sup> Departamento de Física, Universidade Federal de Santa Catarina, P.O. Box 476, 88040-900, Florianópolis, SC, Brazil

<sup>3</sup> Universidade de Sao Paulo, Instituto de Astronomia, Geofísica e Ciências Atmosféricas, Rua do Matao 1226, 05508-090, Sao Paulo, Brazil.

<sup>4</sup> Instituto de Astronomía, Universidad Nacional Autónoma de México, A.P. 70-264, 04510 México D.F., Mexico

<sup>5</sup> INAF-Osservatorio Astrofisico di Arcetri, Largo Enrico Fermi 5, 50125 Firenze, Italy

<sup>6</sup> Depto. de Física Teórica, Universidad Autónoma de Madrid, 28049 Madrid, Spain

<sup>7</sup> Leibniz-Institut für Astrophysik Potsdam (AIP), An der Sternwarte 16, D-14482 Potsdam, Germany

November 23, 2021

## ABSTRACT

We investigate the cosmic evolution of the absolute and specific star formation rate (SFR, sSFR) of galaxies as derived from a spatially-resolved study of the stellar populations in a set of 366 nearby galaxies from the CALIFA survey. The sample spans stellar masses from  $M_{\star} \sim 10^9$  to  $10^{12} M_{\odot}$  and a wide range of Hubble types. The analysis combines GALEX (FUV and NUV) and SDSS (u, g, r, i, z) images with the 4000 Å break, H $\beta$ , and [MgFe] indices measured from the CALIFA data-cubes to constrain parametric models for the star formation history (SFH), which are then used to study the cosmic evolution of the star formation rate density ( $\rho_{\text{SFR}}$ ), the sSFR, the main sequence of star formation (MSSF), and the stellar mass density ( $\rho_{\star}$ ). Several SFH laws are used to fit the observational constraints. A delayed- $\tau$  model,  $\text{SFR} \propto (t_0 - t) \exp(-(t_0 - t)/\tau)$ , provides the best results, in good agreement with those obtained from cosmological surveys. Our main results from this model are: (a) The mass currently in the inner ( $\leq 0.5$  half light radius, HLR) regions formed at earlier epochs than that in the outer (1–2 HLR) regions of galaxies. The time since the onset of the star formation is larger in the inner regions ( $t_0 \sim 13$  to 10 Gyr) than in the outer ones ( $t_0 \sim 11$  to 9 Gyr), for all the morphologies, while the e-folding time-scale  $\tau$  is similar or smaller in the inner than in the outer regions. These results confirm that galaxies of any Hubble type grow inside-out. (b) The sSFR declines rapidly as the Universe evolves, and faster for early than for late type galaxies, and for the inner than for the outer regions of galaxies. (c) The evolution of  $\rho_{\text{SFR}}$  and  $\rho_{\star}$  agrees well with results from cosmological surveys, particularly with the recent results from the GAMA/G10-COSMOS/3D-HST survey. At low redshift,  $z \leq 0.5$ , most star formation takes place in the outer regions of late spiral galaxies, while at  $z > 2$  the inner regions of the progenitors of the current E and S0 are the major contributors to  $\rho_{\text{SFR}}$ . (d) Similarly, the inner regions of galaxies are the major contributor to  $\rho_{\star}$  at  $z > 0.5$ , growing their mass faster than the outer regions, with a lookback time at 50%  $\rho_{\star}$  of  $t_{50} \sim 9$  and 6 Gyr for the inner and outer regions. (e) The MSSF follows a power-law at high redshift, with the slope evolving with time, but always being sub-linear, in good agreement with the *Illustris* simulation. (f) In agreement with galaxy surveys at different redshifts, the average SFH of CALIFA galaxies indicates that galaxies grow their mass mainly in a mode that is well represented by a delayed- $\tau$  model, with the peak at  $z \sim 2$  and an e-folding time of  $\sim 3.9$  Gyr.

**Key words.** Techniques: Integral Field Spectroscopy – galaxies: evolution – galaxies: stellar content – galaxies: structure – galaxies: fundamental parameters – galaxies: bulges – galaxies: spiral

## 1. Introduction

In the last several decades multi-wavelength galaxy surveys have played a key role in the quest to understand how galaxies form and evolve. In particular, surveys at different redshifts have been instrumental to establish that the bulk of the stellar mass ( $M_{\star}$ ) observed today was built up at  $z \geq 2$ . The most relevant observational results are: (1) The star formation rate density in the Universe ( $\rho_{\text{SFR}}$ ) peaks at  $\sim 3.5$  Gyr after the Big Bang, at  $z \sim 2$  (Lilly et al. 1996; Madau et al. 1998; Hopkins & Beacom 2006; Fardal et al. 2007; Madau & Dickinson 2014). (2) The stellar mass density in the Universe ( $\rho_{\star}$ ) evolved very little since  $z \sim 1$  (Pérez-González et al. 2008; Pozzetti et al. 2010; Ilbert et al. 2013; Muzzin et al. 2013). (3) Up to  $z \geq 4$  there exists a relation between SFR and  $M_{\star}$ , known as the main sequence of star formation (MSSF), with a logarithmic slope that is below 1

(Brinchmann et al. 2004; Noeske et al. 2007; Daddi et al. 2007; Elbaz et al. 2007; Wuyts et al. 2011; Whitaker et al. 2012; Renzini & Peng 2015; Tasca et al. 2015; Catalán-Torrecilla et al. 2015a; Cano-Díaz et al. 2016). (4) The specific star formation rate (sSFR = SFR/ $M_{\star}$ ), declines weakly with increasing galaxy mass (Salim et al. 2007; Schiminovich et al. 2007), decreasing rapidly at  $z < 2$  (Rodighiero et al. 2010; Oliver et al. 2010; Karim et al. 2011; Elbaz et al. 2011; Speagle et al. 2014), and increasing slowly at  $z > 2$  (Magdis et al. 2010; Stark et al. 2013; Tasca et al. 2015).

These observational results cannot be easily explained by current models of galaxy formation, which assume that galaxies grow their mass by merging of dark matter halos, progressively assembling more massive systems to become a single massive galaxy (Naab & Ostriker 2016). Moreover, galaxies can grow in a large extent by fresh gas supply from the cosmic web (Kereš

et al. 2005; Dekel et al. 2009a; Lilly et al. 2013). In this context, the gas accretion and SFR are expected to be associated with the specific accretion rate of dark matter (Neistein et al. 2006; Birnboim et al. 2007; Neistein & Dekel 2008; Dutton et al. 2010). However, the specific cosmological accretion rate of baryons declines with time as  $\dot{M}_{acc}/M_{acc} \propto (1+z)^{2.5}$  (Neistein & Dekel 2008; Dekel et al. 2009b), while the observed sSFR  $\propto (1+z)^3$  for galaxies at  $z \leq 2$  (Oliver et al. 2010; Elbaz et al. 2011), and is constant at  $z > 2$  (Magdis et al. 2010; Stark et al. 2013). Some studies have shown that this particular tension can be relaxed assuming different mechanisms, such as enhanced feedback from super-winds in starbursts (Lehnert et al. 2015), or by non-trivial modifications in the semi-analytic models, that involve a suppressed SFR at  $z > 4$  (by enhanced feedback or reduced SFR efficiency) following an initial active phase at  $z > 7$  (Weinmann et al. 2011).

Despite the importance of the high  $z$  work, still much of our knowledge about galaxy evolution comes from the study of nearby galaxies. Surveys at low  $z$  have been very useful to characterize the global properties of galaxies (e.g. Blanton & Moustakas 2009; Kauffmann et al. 2003; Baldry et al. 2010), to retrieve SFR and sSFR as a function of galaxy mass (Brinchmann et al. 2004; Salim et al. 2007; Schiminovich et al. 2007), and the current value of  $\rho_{SFR}$  (Gallego et al. 1995; Brinchmann et al. 2004; Heavens et al. 2004). Moreover, alternatively to surveys at different redshifts, the SFH of the Universe can be inferred by analyzing the fossil record of the current stellar populations of nearby galaxies (Panter et al. 2003; Heavens et al. 2004; Cid Fernandes et al. 2005; Ocvirk et al. 2006; Asari et al. 2007; Panter et al. 2008; Tojeiro et al. 2011; Koleva et al. 2011; McDermid et al. 2015; Citro et al. 2016). This method, that originally started by fitting optical colors of galaxies to study how their SFHs vary along the Hubble sequence (Tinsley 1968, 1972; Searle et al. 1973; Gallagher et al. 1984; Sandage 1986), is currently applied to fit UV-optical integrated spectra of galaxies.

More recently, integral field spectroscopy (IFS) surveys, such as CALIFA (Sánchez et al. 2012; Husemann et al. 2013; García-Benito et al. 2015; Sánchez et al. 2016), ATLAS3D (Cappellari et al. 2011), SAMI (Bryant et al. 2015), and MaNGA (Bundy et al. 2015; Law et al. 2015), allow the study of the spatially-resolved SFH of galaxies from spatially-resolved spectroscopy (Pérez et al. 2013; Cid Fernandes et al. 2014; Sánchez-Blázquez et al. 2014a; González Delgado et al. 2014; Sánchez-Blázquez et al. 2014b; González Delgado et al. 2015; Ibarra-Medel et al. 2016; González Delgado et al. 2016; Goddard et al. 2016; González Delgado et al. 2017; de Amorim et al. 2017; García-Benito et al. 2017; Cortijo-Ferrero et al. 2017; Sanchez et al. 2017; Catalán-Torrecilla et al. 2017). In particular, with CALIFA data and using the non-parametric code `STARLIGHT` (Cid Fernandes et al. 2005; López Fernández et al. 2016), we have obtained the radial distribution of the current SFR and sSFR as a function of Hubble type (González Delgado et al. 2016). We have found that there is a correlation between the stellar mass surface density ( $\mu_*$ ) and the intensity of the star formation ( $\Sigma_{SFR}$ , defined as the SFR per unit area), defining a local MSSF relation with a slope similar to that of the global relation between total SFR and  $M_*$  (González Delgado et al. 2016; Cano-Díaz et al. 2016). This suggests that local processes are important in determining the star formation in disks. Furthermore, the radial profiles of  $\Sigma_{SFR}$  are very similar for all spirals. The radial profiles of current sSFR increase outwards, indicating that the recent shut down of the star formation in spirals is progressing inside-out.

We have also studied the spatially-resolved evolution of the SFR and  $\Sigma_{SFR}$  as a function of galaxy mass and Hubble

type (González Delgado et al. 2017). We have found that: (1) Galaxies form very fast independently of their current stellar mass, with the SFR peaking at  $z \geq 2$ . (2) At any epoch,  $\Sigma_{SFR}$  scales with Hubble type.  $\Sigma_{SFR}$  reaches the highest values ( $> 10^3 M_\odot \text{Gyr}^{-1} \text{pc}^{-2}$ ) in the central regions of current ETGs, similar to those measured in high-redshift star-forming galaxies. SFR increases sub-linearly with  $M_*$ , such that the most massive galaxies have the highest absolute but lowest specific SFRs. (3) Evidence of an early and fast quenching is found only in the most massive ( $M_* > 2 \times 10^{11} M_\odot$ ) E galaxies of the sample, but not in spirals of similar mass, suggesting that halo mass is not the main mechanism for the shut down of star formation. Less massive E and disk galaxies show more extended SFHs and a slower quenching than the massive E.

In this paper we explore a parametric approach to “fossil cosmology”, whereby colors and spectral indices predicted by analytical descriptions of the SFH are fitted to the data and used to obtain the cosmic evolution of  $\rho_{SFR}$ , sSFR, and  $\rho_*$ . We develop a methodology that combines the stellar spectral indexes from CALIFA data with photometry from GALEX and SDSS. In this way, we can harness the power of full spectral fitting (via the more relevant stellar features in the spectra of galaxies) with the spectral energy distribution, by fitting the large baseline of stellar continuum provided by the UV and optical bands. This method makes the results more independent on the errors and uncertainties associated to the calibration of the galaxy spectra.

After verifying that our results are comparable to those inferred from the snapshots of galaxy evolution obtained by studies at different redshifts, we take advantage of the spatially resolved information in our data to investigate how different radial regions contribute to evolution of  $\rho_{SFR}$ , sSFR, and  $\rho_*$ . This is an issue more easily tackled with fossil record studies of nearby galaxies than with redshift surveys, where spatial resolution is observationally challenging. Furthermore, since the morphology of the galaxies in our sample are known, we can also study the role of the currently early and late type galaxies in the evolution of  $\rho_{SFR}$ , sSFR, and  $\rho_*$ .

This work involves a number of assumptions and limitations with respect to studies based on snapshots at different redshifts that need to be mentioned here. Besides limitations related with the fossil record method itself, one should bear in mind that: (a) The Hubble sequence has evolved with time (Delgado-Serrano et al. 2010; Cappellari 2016), so that the progenitors of, say, E and S0 in the local Universe are not necessarily also E and S0 in the past. (b) Due to stellar migrations (Roškar et al. 2008; Minchev et al. 2014), stars currently located at inner and outer regions in a galaxy may not be at these locations in the past. (c) The sample used in this study does not contain galaxies with strong features of interactions or mergers, but such events could well have happened in their past histories. Our analysis cannot say if the mass in a galaxy has grown through mergers or smooth accretion. Mergers do play a role in galaxy evolution (Lotz et al. 2011). It is known, for instance, that the merger rate increases rapidly with redshift (Bundy et al. 2009; Bluck et al. 2009, 2012; López-Sanjuan et al. 2012, 2015; Kaviraj et al. 2015; Rodríguez-Gomez et al. 2015), possibly flattening at  $z > 1$  (Williams et al. 2011; Man et al. 2012; Casteels et al. 2014). The role played by minor or major mergers in setting the current Hubble sequence is still unknown (Lofthouse et al. 2017; Martin et al. 2017).

Notwithstanding these caveats, this study offers relevant insight on how different regions in a galaxy contribute to  $\rho_{SFR}(t)$ , sSFR( $t$ ), and  $\rho_*(t)$ , as well as how galaxy morphology relates to this cosmic evolution.

This paper is organized as follows. Section 2 describes the observations and properties of the galaxies analyzed here. In Sections 3 and 4 we explain our method and present the results of the SFH analysis. In Section 5 we use these results to estimate the cosmic evolution of  $\rho_{\text{SFR}}$ , sSFR, and  $\rho_{\star}$  and to compare them with results obtained from surveys at different redshifts. Section 6 then examines how present day morphology, and how inner and outer galaxy regions contribute to the  $\rho_{\text{SFR}}(t)$ , sSFR( $t$ ), and  $\rho_{\star}(t)$  budget. The evolution of the MSSF is also discussed. Section 7 reviews our main findings. We adopt a flat cosmology for the relation between lookback time,  $t(z)$ , and redshift:  $\Omega_M = 0.3$ ,  $\Omega_{\Lambda} = 0.7$ , and  $H_0 = 70 \text{ km s}^{-1} \text{ Mpc}^{-1}$ . The units of  $M_{\star}$  are  $M_{\odot}$  throughout; we do not specify them for the sake of clarity.

## 2. Sample and data

### 2.1. Sample

The main characteristics of the CALIFA mother sample are: (a) angular isophotal diameter between  $45''$  and  $79''$ ; (b) redshift range  $0.005 \leq z \leq 0.03$ ; (c) color ( $u - r < 5$ ) and magnitude ( $-24 < M_r < -17$ ) covering the whole color-magnitude diagram. A full description and characterization of the mother sample is given by Walcher et al. (2014). Although the sample is not limited in volume, it can be "volume-corrected", allowing us to provide estimates of the stellar mass function (Walcher et al. 2014) and other cosmological observables such as  $\rho_{\text{SFR}}$  (González Delgado et al. 2016). The volume-corrected distribution functions of luminosities, masses, and sizes are statistically compatible with estimates from the full SDSS when accounting for large-scale structure (see figures 8, 9, and 14 in Walcher et al. 2014).

The sample used in this study comprises all the galaxies from the CALIFA survey (Sánchez et al. 2012, 2016) with COMBO cubes (the combination of the observations with the V1200 and V500 setups) in the data release 2 (García-Benito et al. 2015) for which there are GALEX images available (Martin et al. 2005). This sub-sample comprises 366 galaxies, and is representative of the full CALIFA mother sample, covering seven bins in morphology: E (54), S0 (48), Sa (66), Sb (58), Sbc (63), Sc (58) and Sd (19). Fig. 1 shows that these proportions are very similar to the ones in the mother sample. In terms of stellar masses, our sub-sample runs from  $\log M_{\star} = 8.6$  to 11.9 (for a Chabrier IMF).

### 2.2. Observations and data reduction

The observations were carried out at the Calar Alto observatory with the 3.5m telescope and the Potsdam Multi-Aperture Spectrometer PMAS (Roth et al. 2005) in the PPaK mode (Verheijen et al. 2004). PPaK is an integral field spectrograph with a field of view of  $74'' \times 64''$  and 382 fibers of  $2.7''$  diameter each (Kelz et al. 2006). We use data calibrated with the version 1.5 of the reduction pipeline García-Benito et al. (2015). The spectra cover the  $3700\text{--}7300 \text{ \AA}$  range with the same resolution as the V500 grating ( $\sim 6 \text{ \AA}$  of FWHM) and a spatial sampling of 1 arcsec/spaxel.

GALEX images at FUV ( $\lambda_{\text{eff}} \sim 1542 \text{ \AA}$ ) and NUV ( $\lambda_{\text{eff}} \sim 2274 \text{ \AA}$ ) bands were retrieved from the GALEX website<sup>1</sup>. We use the calibrated data products by Morrissey et al. (2007), but we did the sky subtraction by averaging the intensity in several regions of the images. Galactic extinction was corrected for with

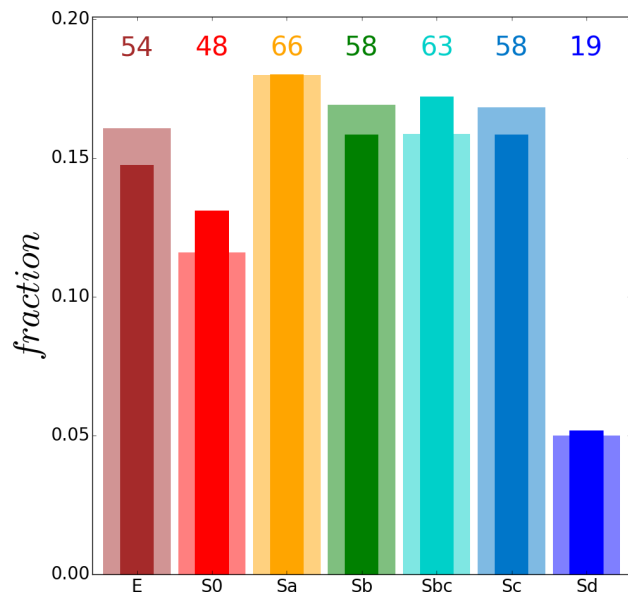


**Fig. 1.** Comparison of Hubble type distributions in the CALIFA mother sample (939 galaxies, broad bars) and the 366 galaxies analyzed here (narrow, darker bars). Both histograms are normalized to unit sum. The number of galaxies in each morphology bin is labeled in color.

$A_{\lambda}/E(B - V) = 8.24$  and  $8.20$ , for FUV and NUV respectively (Wyder et al. 2007).

Calibrated u, g, r, i, and z images from the 10<sup>th</sup> SDSS data release (Ahn et al. 2014) were retrieved from the SDSS website<sup>2</sup>. To correct for Galactic extinction we use the conversion from  $E(B - V)$  to total extinction  $A_{\lambda}$  tabulated by Stoughton et al. (2002), namely:  $A_{\lambda}/E(B - V) = 5.155, 3.793, 2.751, 2.086, 1.479$  for filters u, g, r, i, and z, respectively. These corrections, and those done on the FUV and NUV bands, are compatible with the Galactic extinction corrections applied to the CALIFA data cubes (García-Benito et al. 2015).

The MONTAGE software<sup>3</sup> was used to perform a resampling of the SDSS and GALEX images to the same spatial scale as CALIFA, and also to align and cut the GALEX images using WCS to obtain processed FUV and NUV images with the same FoV as our CALIFA datacubes.

Because of the inferior spatial resolution of the UV images with respect to the optical images and spectra, the spatial analysis is reduced by analyzing only three radial regions: (i) between  $R = 0$  and 2 HLR (the whole galaxy), (ii) inside  $R < 0.5$  HLR (the central region, dominated by the galaxy bulge), and (iii) between  $R = 1$  and 2 HLR, where HLR denotes the galaxy's Half Light Radius, measured as in Cid Fernandes et al. (2013).

The spectral indices described in 3.1 were measured from CALIFA spectra extracted within these three apertures. Fluxes in the NUV, FUV, and ugriz images were measured in the same regions, after masking foreground stars and low signal-to-noise regions masked in the CALIFA data.

<sup>2</sup> skyserver.sdss.org

<sup>3</sup> http://montage.ipac.caltech.edu

<sup>1</sup> https://asd.gsfc.nasa.gov/archive/galex

### 3. Star formation history analysis

The method to derive the star formation history for each spectrum consists in finding out the best parameters of an analytical model for the SFH that fits simultaneously a combination of UV+optical photometry from GALEX and SDSS and spectral indices from CALIFA data.

#### 3.1. Observational constraints and stellar population models

In addition to the GALEX FUV and NUV photometry and SDSS ugriz photometry, we measure the  $H\beta$  index, the 4000 Å break  $D_n4000$ , and  $[MgFe]'$  in the CALIFA spectra. We use the Lick index definition (Worthey 1994) for  $H\beta$ , and Balogh et al. (1999) for  $D_n4000$ . These are both good indicators of the stellar population age (Bruzual & Charlot 2003; Kauffmann et al. 2003; González Delgado et al. 2005).  $[MgFe]'^4$  is a good tracer of the stellar metallicity in a galaxy ( $Z_*$ ). The advantage of this index with respect to other  $Z_*$ -indicators (such as Mgb) is that it is almost independent of the  $\alpha/Fe$  ratio (Thomas et al. 2003).

While  $[MgFe]'$  and  $D_n4000$  are measured directly in the CALIFA spectra, the  $H\beta$  index needs to be corrected for nebular emission. In practice, we use the synthetic value of the index obtained from a full spectral fit with STARLIGHT (Cid Fernandes et al. 2005).

To model these 10 observables (7 photometric points plus three spectral indices) we use spectral models for simple stellar populations (SSP) from an updated version of the Bruzual & Charlot (2003) models (Charlot & Bruzual 2007, private communication<sup>5</sup>), where the STELIB spectral library (Le Borgne et al. 2003) is replaced by a combination of the MILES (Sánchez-Blázquez et al. 2006; Falcón-Barroso et al. 2011) and GRANADA (Martins et al. 2005) libraries. This set of models is one denoted as base *CBe* in our previous works (González Delgado et al. 2015, 2016). The evolutionary tracks are those collectively known as Padova 1994 (Alongi et al. 1993; Bressan et al. 1993; Fagotto et al. 1994a,b; Girardi et al. 1996). The IMF is that of Chabrier (2003). The metallicity covers  $\log Z_*/Z_\odot = -2.3, -1.7, -0.7, -0.4, 0, \text{ and } +0.4$ , while ages run from 0 to 14 Gyr. The spectrum produced by one such SSP of initial mass  $1M_\odot$  is denoted by  $SSP_\lambda(t, Z)$ .

These models are combined with a parametric prescription for the SFH and a simple recipe for the effects of dust to predict the observables listed above. This process is similar to that followed by Gallazzi et al. (2006) to retrieve the stellar population properties of galaxies in the SDSS survey, and, more recently, by Zibetti et al. (2017) for CALIFA data.

#### 3.2. Method

##### 3.2.1. General aspects

We assume a generic SFH = SFH( $t; \Theta$ ), where  $t$  is the lookback time and  $\Theta$  is a vector of parameters including the stellar metallicity ( $Z_*$ ), a dust attenuation parameter ( $\tau_V$ ), and parameters controlling the temporal behavior of the SFR  $\psi(t)$ . For instance, in a conventional ‘tau-model’  $\psi(t)$  decays exponentially from an initial value  $\psi_0$  at time  $t_0$ , with  $\psi(t) = \psi_0 e^{-(t_0-t)/\tau}$ , where  $\tau$  is SFR e-folding time. This particular model (one of the many we experimented with; see Appendix A.2) is characterized by five parameters:  $\Theta = (\psi_0, t_0, \tau, Z_*, \tau_V)$ .

<sup>4</sup> A combination of the Lick indices Mgb, Fe5270, and Fe5335 (Thomas et al. 2003)

<sup>5</sup> <http://www.bruzual.org/~gbruzual/cb07>

The synthetic spectrum for a given parameterization and choice of  $\Theta$  is computed with

$$L_\lambda(\Theta) = e^{-q_\lambda \tau_V} \int SSP_\lambda(t, Z) \psi(t; \Theta) dt, \quad (1)$$

where  $q_\lambda \equiv \tau_\lambda/\tau_V$  denotes the attenuation law which, in our case, is the one by Calzetti et al. (2000).

The goal is to explore the parameter space and constrain the parameters  $\Theta$  that fit our data (indices + photometry). We use a Markov chain Monte Carlo (MCMC) method to sample the parameter space. For each sampled  $\Theta$  we:

- Compute the predicted model spectrum (equation 1) for a SFH forming a total of  $1M_\odot$  in stars.
- Evaluate the corresponding observables.
- Determine the corresponding total stellar mass formed by maximizing the likelihood of the scale dependent observables (the photometric fluxes, in our case).
- Compare the observed and model observables, obtaining the likelihood of the data given  $\Theta$ .

In what follows we explain how this general method is implemented in practice.

##### 3.2.2. Bayesian inference

Given a set of observations  $O$  (7 broad band magnitudes and 3 spectral indices in our case), the general goal of an MCMC algorithm is to draw a set of samples  $\{\Theta_i\}$  in the parameter space from the posterior probability density

$$p(\Theta|O) = \frac{p(\Theta)p(O|\Theta)}{p(O)}, \quad (2)$$

where  $p(\Theta)$  is the prior distribution on  $\Theta$  and  $p(O|\Theta)$  is the likelihood function. The normalization  $p(O)$  is independent of  $\Theta$  once we have chosen the form of the generative model, and therefore it can be omitted from the analysis.

An advantage of a Bayesian analysis is that we can marginalize over uninteresting parameters. In our case we are more interested on parameters controlling the temporal behavior of the SFH than on  $Z_*$  or  $\tau_V$ . Moreover, once the MCMC sample of  $p(\Theta|O)$  is available we can also obtain the expected value of any function of  $\Theta$ . For example, the expected value of the luminosity-weighted mean log stellar age is computed from

$$\langle \log t \rangle_L = \sum_{\Theta_i} p(\Theta_i|O) \langle \log t \rangle_L(\Theta_i) \quad (3)$$

where  $\langle \log t \rangle_L(\Theta_i)$  is the mean age for a particular  $\Theta_i$  and the sum runs over all  $\Theta_i$ 's sampled by the MCMC.

The formalism is also useful to evaluate typical uncertainties on the model parameters. For example, the uncertainties in  $t_0$  and  $\tau$  are calculated as:

$$\langle t_0 \rangle = \sum_{t_0} p(t_0|O) t_0; \quad \sigma_{\langle t_0 \rangle}^2 = \sum_{t_0} p(t_0|O) [t_0 - \langle t_0 \rangle]^2 \quad (4)$$

$$\langle \tau \rangle = \sum_{\tau} p(\tau|O) \tau; \quad \sigma_{\langle \tau \rangle}^2 = \sum_{\tau} p(\tau|O) [\tau - \langle \tau \rangle]^2 \quad (5)$$

These estimates can then be propagated to estimate the associated uncertainties in properties such as  $\rho_{\text{SFR}}$  and  $\rho_*$ , as done in Sections 5.1 and Sec. 5.3.

### 3.2.3. Likelihood function

Assuming gaussian errors,  $p(O|\Theta) \propto e^{-\chi^2(\Theta)/2}$ , so the computation of the likelihood  $p(O|\Theta)$  reduces to the evaluation of the corresponding  $\chi^2(\Theta)$ , which in our case splits into two parts: One  $\chi^2$  related to the  $N_{\text{mag}} = 7$  photometric magnitudes and another one related to the  $N_{\text{Lick}} = 3$  Lick indices. The latter reads

$$\chi_{\text{Lick}}^2 = \sum_{j=1}^{N_{\text{Lick}}} \left( \frac{I_j^{\text{obs}} - I_j^{\text{mod}}(\Theta)}{\epsilon(I_j^{\text{obs}})} \right)^2, \quad (6)$$

where  $I_j^{\text{obs}}$  and  $\epsilon(I_j^{\text{obs}})$  denote the observed index and its uncertainty, and  $I_j^{\text{mod}}(\Theta)$  is the predicted value for the SFH parameters encoded in  $\Theta$ .

The photometric component of  $\chi^2(\Theta)$  is

$$\chi_{\text{mag}}^2 = \sum_{j=1}^{N_{\text{mag}}} \left( \frac{O_j - M_j(\Theta; 1M_{\odot}) - A(\Theta)}{\epsilon(O_j)} \right)^2 \quad (7)$$

where  $O_j$  and  $\epsilon(O_j)$  are the observed magnitude and its error,  $M_j(1M_{\odot})$  is the magnitude expected for a galaxy forming  $1M_{\odot}$  in stars, and  $A = -2.5 \log M_{\star}'$  defines the optimal<sup>6</sup> mass formed in stars ( $M_{\star}'$ ) for parameters  $\Theta$ .

We combine  $\chi_{\text{Lick}}^2$  and  $\chi_{\text{mag}}^2$  as follows:

$$\chi_{\text{tot}}^2 = \chi_{\text{mag}}^2 + \frac{N_{\text{mag}}}{N_{\text{Lick}}} \chi_{\text{Lick}}^2. \quad (8)$$

where the factor  $N_{\text{mag}}/N_{\text{Lick}} = 7/3$  scales the two  $\chi^2$ 's to give the same weight to magnitudes and indices. Typically, the assumed errors in the magnitudes are 0.08, 0.06, 0.07, 0.05, 0.05, 0.05 and 0.06 mag, for FUV, NUV, u, g, r, i, z respectively. For the indices, the average errors are: 0.14 Å, 0.09, and 0.03 Å, for H $\beta$ , D $_n$ 4000, and [MgFe]', respectively.

## 4. Star formation histories as a function of Hubble type and radial region

This section presents our results for the SFH as a function of the Hubble type and galaxy mass. We discuss the absolute and specific SFR, and mass fraction as a function of lookback time. The spatial analysis is simplified to three radial regions:  $R = 0$ –2 HLR,  $R < 0.5$  HLR, and  $R = 1$ –2 HLR, corresponding to the whole-galaxy, the central region (dominated by the galaxy bulge), and outer regions (dominated by the disk). First we present our reference SFH law, the quality of the fits, and the stellar population properties obtained from the integrated spectra.

### 4.1. The delayed- $\tau$ model

We have explored a total of nine different parameterizations for  $\psi(t; \Theta)$ . Appendix A.2 describes and compares these alternative models. In what follows we restrict our discussion to the results obtained with a delayed- $\tau$  model:

$$\psi(t) = k \frac{(t_0 - t)}{\tau} e^{-(t_0 - t)/\tau} \quad (9)$$

where  $t$  is the lookback-time,  $t_0$  is the lookback-time onset of the star formation,  $\tau$  is the SFR e-folding time and  $k$  is a normalization factor trivially related to the total mass formed in stars,  $M_{\star}' = \int \psi(t) dt$ . Although not as popular as a simple exponential decay, this recipe has been used in several works (e.g., Bruzual A. & Kron 1980; Chiosi 1980; Gavazzi et al. 2002; Chiosi et al. 2017; Lee et al. 2010; Simha et al. 2014).

This model involves a total of four parameters,  $\Theta = (t_0, \tau, Z, \tau_V)$ , plus the stellar mass  $M_{\star}$  which is optimized as explained in the previous section. To quantify how well the model fits the data we may use the difference between the synthetic and observed quantity in units of its error:  $\Delta \equiv (\text{model} - \text{data})/\text{error}$ . The mean and one sigma values of  $\Delta$  for the three spectral indices are  $0.56 \pm 0.60$ ,  $-0.38 \pm 1.06$ ,  $0.66 \pm 0.94$  for D $_n$ 4000, [MgFe]', and H $\beta$ , respectively, indicating satisfactory fits. The same is true for the SDSS magnitudes, with  $\Delta = 0.19 \pm 1.15$ ,  $-0.08 \pm 0.71$ ,  $-0.46 \pm 0.29$ ,  $-0.30 \pm 0.28$  and  $0.10 \pm 0.55$  for u, g, r, i, and z, respectively. The GALEX bands are the least well fitted observables, with  $\Delta_{\text{FUV}} = -1.38 \pm 0.81$  and  $\Delta_{\text{NUV}} = 1.84 \pm 0.98$ . As shown in the Appendix, these differences between the observed and predicted UV fluxes are reduced only when a combination of two exponential functions is used for  $\psi(t)$ .

The quality of the fits obtained with the delayed- $\tau$  model is similar to those obtained with exponential or Sandage (1986) models for the SFH; in terms of  $\chi^2$ , the best is a combination of two SFH models (see Fig. A.3). Nevertheless, we favor the delayed- $\tau$  model because it results in a better match of the cosmic evolution of published  $\rho_{\text{SFR}}$  and sSFR from galaxy surveys.

For each galaxy, this analysis provides estimates of  $t_0$ ,  $\tau$ ,  $Z_{\star}$ ,  $\tau_V$ , and  $M_{\star}$ , as well as the associated SFR( $t$ ) and sSFR( $t$ ) functions. Other properties, such as the mean stellar ages and metallicities, can be derived from these. In what follows we explore the results of these SFH fits. The emphasis is on statistical results obtained when grouping galaxies by their Hubble type.

### 4.2. Global properties as a function of Hubble type

In Fig. 2 we present the results for the stellar mass ( $M_{\star}$ ), attenuation ( $\tau_V$ ), luminosity-weighted age ( $\langle \log t \rangle_L$ ), and the stellar metallicity ( $\langle \log Z \rangle$ )<sup>7</sup>, as a function of Hubble type. Dots represent the expected values (cf. equation 3) for individual galaxies, while and coloured stars mark the average for each morphology bin.

As noticed in our previous works,  $M_{\star}$  correlates with Hubble type, with average values of  $\log M_{\star} = 11.18, 10.98, 10.81, 10.80, 10.51, 9.97$ , and  $9.85$  for E, S0, Sa, Sbc, Sc, and Sd, respectively. Extinction is not correlated with morphology, but spirals have higher  $\tau_V$  than E and S0.  $\langle \log t \rangle_L$  and  $\langle \log Z \rangle$  scale with the Hubble type, with early type galaxies (ETG) more metal rich and older than late type spirals.

These trends with the Hubble type are in good agreement with those derived by González Delgado et al. (2014, 2015) using STARLIGHT for the non-parametric spectral fits instead of the parametric models used in this paper. The agreement is also quantitative when the SSP models used for the full spectral fits are the same ones used for the parametric analysis. The differences between non-parametric and parametric properties are

<sup>7</sup> For this model, the metallicity is calculated as:

$$\langle \log Z \rangle = \sum_{\Theta_i} p(\Theta_i|O) \log Z_{\star}(\Theta_i) \quad (10)$$

<sup>6</sup> optimal in the sense of  $\partial \chi_{\text{mag}}^2 / \partial M_{\star}' = 0$  (see Walcher et al. 2011)

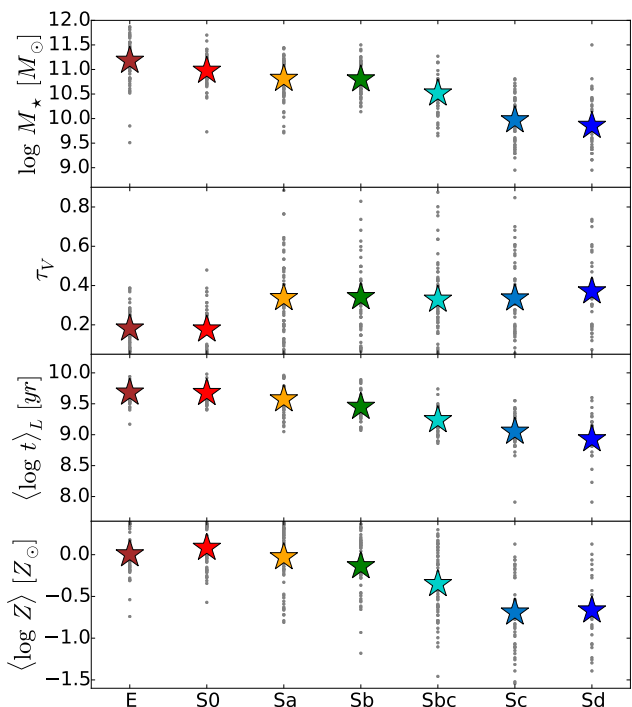


**Fig. 2.** Global stellar population properties as a function of the Hubble type obtained with a delayed- $\tau$  model and Chabrier IMF. From top to bottom are the galaxy stellar mass ( $M_*$ ), attenuation ( $\tau_V$ ), light-weighted averaged age ( $\langle \log t_L \rangle$ ), and stellar metallicity ( $\langle \log Z \rangle$ ). The individual galaxy values are plotted as grey dots, and the average values for each Hubble type as color coded stars.

(mean  $\pm$  standard deviation)  $0.16 \pm 0.17$  in  $\log M_*$ ,  $-0.12 \pm 0.12$  in  $\tau_V$ ,  $0.12 \pm 0.20$  in  $\langle \log t_L \rangle$ , and  $-0.07 \pm 0.37$  in  $\langle \log Z \rangle$ .

We note that in a few cases our parametric fits produce unrealistically small values of  $t_0$ . For 4 of our 54 E galaxies, for instance, the fits suggest  $t_0 \sim 4$  Gyr and small  $\tau$  values. These objects are better represented by a combination of an old population with some modest recent star formation, a mixture that is not well described by a delayed- $\tau$  model. This difficulty is analogous to the one described by Trager et al. (2000), who find that single burst models for early type galaxies sometimes find too young ages, and that a more reasonable scenario is one where a "frosting" of young stars is added to an old "base" population (see also Kaviraj et al. (2007)). Overall, these cases are not numerous enough to affect our main results.

#### 4.3. The evolution of the star formation rate

Figure 3 shows the time evolution of the SFR for seven morphology bins obtained for the global ( $R \leq 2$  HLR, left panel), central ( $R \leq 0.5$  HLR, middle panel), and outer regions ( $1 \leq R \leq 2$  HLR, right panel) of the galaxy. In order to make a consistent comparison with results obtained with non-parametric methods (such as those obtained with STARLIGHT, see figure 6 in González Delgado et al. 2017), we compute the mean star formation history for each Hubble type by averaging the SFR( $t$ ) functions for individual galaxies in the same morphology group. The error in the mean is computed as the r.m.s. dispersion of the correspond-

ing SFR( $t$ ) values divided by the square root of the number of galaxies in each bin.

These statistics are computed after excluding the 5% of objects with smaller  $t_0$  in each group. This minor correction is done only for cosmetic purposes. Since these outliers also have small  $\tau$  values, their SFHs are concentrated in time, leading to artificial peaks in the mean SFR( $t$ ) curves, which are meant to be typical of a given morphology group.

Figure 3 shows that the SFRs at any epoch scale with the Hubble type, as expected due to the relations between SFR,  $M_*$ , and morphology. E galaxies have the highest SFRs, reaching  $\sim 40 M_\odot \text{ yr}^{-1}$  about 9 Gyr ago ( $z \sim 1.5$ ), while the lowest SFRs at the same epoch occur in Sd galaxies, with only  $\sim 3 M_\odot \text{ yr}^{-1}$ . Note that although the shape of SFR( $t$ ) for each individual galaxy follows a delayed- $\tau$  function, the mean SFR( $t$ ) curve does not. This happens because of the dispersion on the fitted  $t_0$  and  $\tau$  among galaxies in a same Hubble type bin. The end result is that the mean SFR( $t$ ) curves show a relatively broad plateau from  $z \sim 2$  to 1, as well as some secondary peaks. This is evident not only for E, but also for S0 and late type spirals. At recent epochs, the SFRs have declined by a factor of  $\sim 40$  for ETG, and  $\sim 2$  for Sc with respect to their values at  $z \sim 1-2$ .

The SFR in the inner regions (central panel) increases faster at earlier times and declines quickly after the peak, in particular for E's. At the peak of the star formation epoch (lookback time 10-12 Gyr) the inner region contributes significantly ( $\sim 55\%$ ) to the total SFR. In contrast, for the Sd galaxies, the  $R < 0.5$  HLR region accounts for only 16% of the total SFR.

The SFR in the outer regions (right panel) of spirals shows a behavior similar to that in the inner regions, but with a rising phase that extends to more recent times, and a declining phase that is also more extended in time. In ETG's, and in particular E's, the peak of star formation occurs between redshift 1 and 0.5. This result confirms our previous suggestion that E galaxies are actively forming or accreting stars in the outer regions between  $\sim 5$  and 8 Gyr ago (González Delgado et al. 2017).

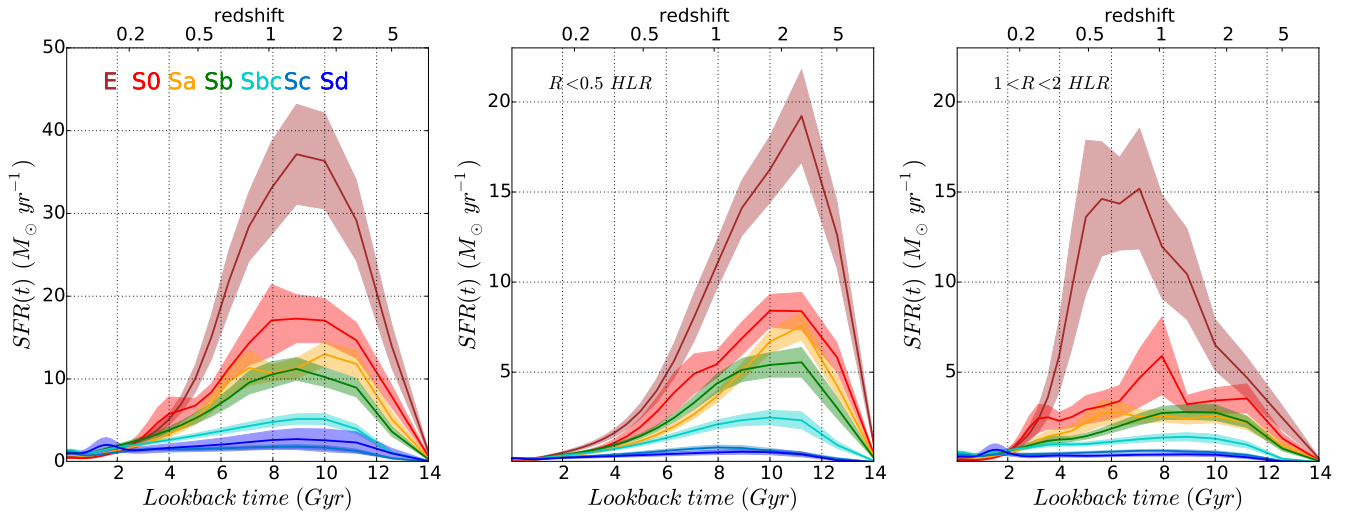
#### 4.4. The star formation rate parameters

Table 1 and Fig. 4 shows the statistics (mean and standard deviation) for all values  $t_0$  and  $\tau$  as a function of Hubble type and radial region. Because the 5% of outliers (excluded from Fig. 3) are included in the statistics, the dispersion in  $t_0$  is significant, in particular for E galaxies. The average values indicate that the onset of star formation occurs very early on: In Sd,  $t_0 \sim 9$  Gyr; in Sc,  $t_0 \sim 10$  Gyr; in Sa-Sb  $t_0 \sim 12$  Gyr, and in E and S0  $t_0 \sim 10.1 - 10.7$  Gyr. The onset of star formation in the inner regions is earlier than in the outer regions, i.e.,  $t_0(R < 0.5) > t_0(1 < R < 2)$ .

The time scale  $\tau$  increases from 1.4 Gyr in E to 4.1 Gyr in Sc, indicating that the period of star formation is more extended in late spirals than in ETG. The outer regions of spirals have a larger e-folding time than the inner regions,  $\tau(R < 0.5) < \tau(1 < R < 2)$ ; for instance, Sc galaxies typically have  $\tau = 5.3$  Gyr at  $1 < R < 2$  HLR, but 3.6 Gyr at  $R < 0.5$  HLR. In ETGs the inner and outer values are quite similar, with  $\tau \sim 1.2$  and 1.5 Gyr, respectively.

These results confirm our earlier finding that galaxies form inside-out (Pérez et al. 2013; González Delgado et al. 2014, 2015; García-Benito et al. 2017), because the peak of star formation, at  $t = t_0 - \tau$ , always occurs earlier in the inner than in the outer regions, and this inner-outer delay is very similar in all Hubble types, with  $(t_0 - \tau)_{inner} - (t_0 - \tau)_{outer} = 2.2$  Gyr on average.





**Fig. 3.** The evolution of the star formation rate (SFR) of CALIFA galaxies as a function of Hubble type; for the whole galaxy (left), the inner (middle), and outer regions (right). Solid lines are the average  $sSFR(t)$  of the galaxies in each morphology bin removing only the 5% of galaxies with smallest  $t_0$ . Shaded bands around the average curves represent  $\pm$  the error in the mean.

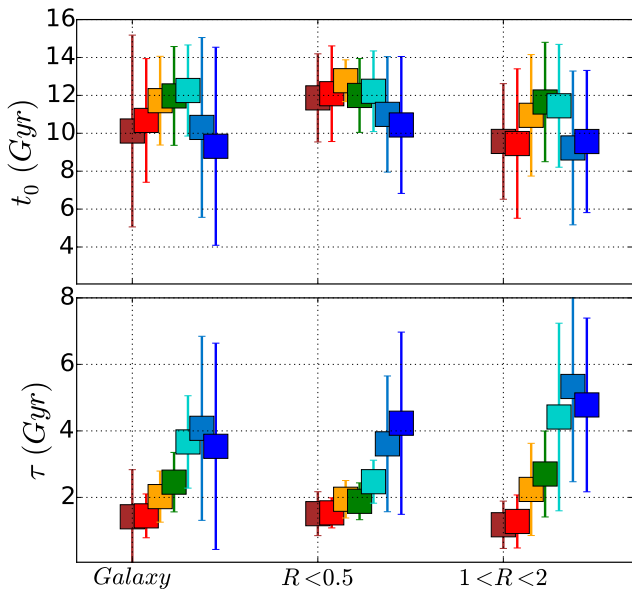


**Fig. 4.** Average and dispersion of the parameters  $t_0$  and  $\tau$  of a delayed- $\tau$  model for the SFH, grouped into seven morphology bins. The three columns refer to results obtained for the whole galaxy (left), only the central  $R < 0.5$  HLR regions (middle), and  $1 < R < 2$  HLR (right).

#### 4.5. The evolution of the specific star formation rate

The SFH of a galaxy can be expressed also through the time evolution of its specific star formation rate (sSFR), defined as the ratio between the current SFR and the stellar mass,  $sSFR = SFR(t=0)/M_*(t=0)$ . This quantity provides information of the relative rate at which stars are forming now with respect to the past. The  $sSFR(t=0)$  declines slowly with increasing  $M_*$  because the MSSF is sublinear ( $SFR \sim M_*^\alpha$ , with  $\alpha = 0.7-0.9$ , Brinchmann et al. 2004; Salim et al. 2004; Renzini & Peng 2015; Catalán-Torrecilla et al. 2015b; González Delgado et al. 2016).

	M1 model	$t_0$ [Gyr]	$\tau$ [Gyr]
E	$R < 0.5$	$11.9 \pm 2.3$	$1.5 \pm 0.7$
	galaxy	$10.1 \pm 5.1$	$1.4 \pm 1.4$
	$1 < R < 2$	$9.6 \pm 3.1$	$1.2 \pm 0.7$
S0	$R < 0.5$	$12.1 \pm 2.5$	$1.5 \pm 0.5$
	galaxy	$10.7 \pm 3.3$	$1.4 \pm 0.7$
	$1 < R < 2$	$9.5 \pm 3.9$	$1.3 \pm 0.8$
Sa	$R < 0.5$	$12.8 \pm 1.1$	$1.9 \pm 0.6$
	galaxy	$11.7 \pm 2.3$	$2.0 \pm 0.8$
	$1 < R < 2$	$10.9 \pm 3.2$	$2.2 \pm 1.4$
Sb	$R < 0.5$	$12.0 \pm 2.0$	$1.9 \pm 0.5$
	galaxy	$12.0 \pm 2.6$	$2.5 \pm 0.9$
	$1 < R < 2$	$11.6 \pm 3.1$	$2.7 \pm 1.9$
Sbc	$R < 0.5$	$12.2 \pm 2.1$	$2.5 \pm 0.6$
	galaxy	$12.3 \pm 2.4$	$3.7 \pm 1.4$
	$1 < R < 2$	$11.4 \pm 3.2$	$4.4 \pm 2.8$
Sc	$R < 0.5$	$11.0 \pm 3.0$	$3.6 \pm 2.0$
	galaxy	$10.3 \pm 4.7$	$4.1 \pm 2.8$
	$1 < R < 2$	$9.2 \pm 4.1$	$5.3 \pm 2.9$
Sd	$R < 0.5$	$10.4 \pm 3.6$	$4.2 \pm 2.7$
	galaxy	$9.3 \pm 5.2$	$3.5 \pm 3.1$
	$1 < R < 2$	$9.6 \pm 3.7$	$4.8 \pm 2.6$

**Table 1.** Average and standard deviation of  $t_0$  and  $\tau$ , the SFH parameters for a delayed- $\tau$  model (eq. 9) for seven bins in Hubble type. For each type we list the results obtained for the integrated spectra, and for spectra that include regions located at  $R < 0.5$  HLR and  $1 < R < 2$  HLR.

In previous works, using the fossil record analysis based on the full spectral fitting of CALIFA data with STARLIGHT, we were able to: (a) map the radial structure of the  $sSFR(t=0)$ , and (b) study temporal variations of the  $sSFR$ . Our analysis has shown that  $sSFR$  decreases as the Universe evolves (González Delgado et al. 2017), in line with redshift surveys (Speagle et al. 2014).

One important advantage of the methodology proposed here based on parametric SFH is that for each galaxy we have an analytical expression for  $SFR(t)$  (eq. 9), and the values of the  $sSFR(t)$  are more easily derived. The  $sSFR(t)$  for each galaxy is calculated as  $SFR(t)/M_*(t)$ , where the SFR at each epoch is di-

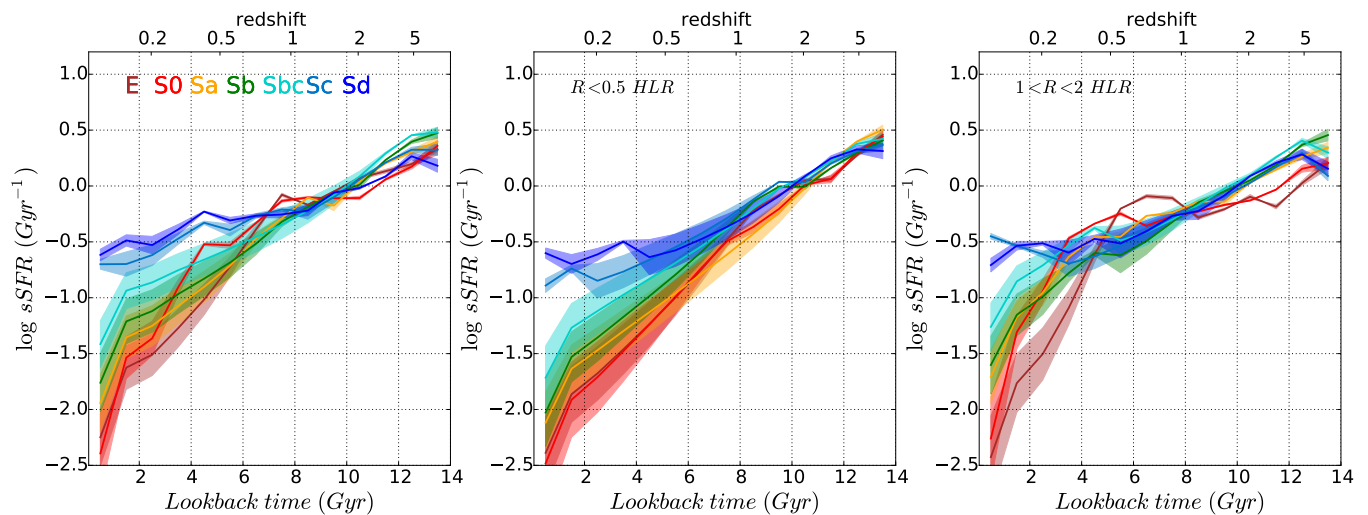


**Fig. 5.** As Fig. 3, but showing the evolution of the specific star formation rate.

vided by  $M_{\star}(t)$  (the stellar mass of the galaxy at lookback time  $t$ ), estimated as:

$$M_{\star}(t) = \int_{t_0}^t (1 - R(t)) \text{SFR}(t) dt \quad (11)$$

where the original mass formed in stars,  $\int_{t_0}^t \text{SFR}(t) dt$ , is corrected by the mass loss term  $R(t)$ . Rather than assuming a global correction, we use the prediction given by the SSP models (Bruzual & Charlot 2003) for each population of each galaxy, based on their ages and metallicities. Then, the individual sSFR( $t$ ) are stacked as a function of Hubble type.

Figure 5 shows our results, where the full lines are average curves and shaded bands are  $\pm$  the error in the mean, i.e., the dispersion divided by the square root of the number of galaxies in each class. For all morphological types the sSFR( $t$ ) curves decrease as the Universe evolves, but the slope is different for each Hubble type. Sd galaxies have the flattest slope, while Sa, S0 and E show steeper slopes.

The middle panel in Fig. 5 shows the sSFR( $t$ ) of regions located in the central 0.5 HLR. Although the behavior is similar to that of the whole galaxy, the slope is steeper, producing the shut-down of the star-formation at earlier epochs. At  $z > 2$ , all the galaxies seem to have a common sSFR( $t$ ) of  $\sim 2 \text{ Gyr}^{-1}$ . In contrast, for regions currently located in the disk of spirals, sSFR( $t$ ) declines more slowly (right panel in Fig. 5), indicating a longer period of star formation. The outer regions of E galaxies show a remarkable behavior: over the period  $0.5 \leq z \leq 1$ , sSFR( $t$ ) run above those of spirals, while at  $z > 1$  they are below. In previous works we suggested this period  $0.5 < z < 1$  as an epoch of growth of the envelope of E and S0 through mergers.

## 5. Comparison with galaxy redshift surveys

We now put the SFHs presented in the last section in a cosmic context by applying volume corrections to obtain  $\rho_{\text{SFR}}(t)$ , sSFR( $t$ ), and  $\rho_{\star}(t)$ . Our main goals in this section are: 1) To compare our results for the cosmic evolution of the SFR, sSFR and stellar mass obtained from the analysis of CALIFA data corresponding to the whole galaxy with the results from redshift surveys in the literature. These comparisons allow us to establish the advantages and also the limitations of the fossil record

$\log \rho_{\text{SFR}} [M_{\odot} \text{yr}^{-1} \text{Mpc}^{-3}]$		$z = 0$	$z = 1$	$z = 2$	$z = 5$
<b>MI</b>	$R < 0.5$	$-2.61 \pm 0.13$	$-1.89 \pm 0.11$	$-1.72 \pm 0.09$	$-1.70 \pm 0.08$
	Galaxy	$-2.04 \pm 0.38$	$-1.39 \pm 0.14$	$-1.34 \pm 0.07$	$-1.41 \pm 0.12$
	$1 < R < 2$	$-2.40 \pm 0.11$	$-1.89 \pm 0.31$	$-1.93 \pm 0.14$	$-2.09 \pm 0.25$
Driver et al.		-1.94	-1.31	-1.30	-1.46
Madau & Dickinson		-2.05	-1.27	-1.10	-1.41
Fardal et al.		-2.28	-1.42	-1.35	
$\log \text{sSFR} [\text{Gyr}^{-1}]$		$z = 0$	$z = 1$	$z = 2$	$z = 5$
<b>MI</b>	$R < 0.5$	$-1.59 \pm 0.04$	$-0.34 \pm 0.02$	$-0.06 \pm 0.03$	$0.13 \pm 0.02$
	Galaxy	$-1.27 \pm 0.13$	$-0.27 \pm 0.04$	$-0.08 \pm 0.12$	$0.18 \pm 0.02$
	$1 < R < 2$	$-1.16 \pm 0.05$	$-0.36 \pm 0.03$	$-0.13 \pm 0.02$	$0.08 \pm 0.02$
Elbaz et al.		-1.12	-0.21	0.18	
$\log \rho_{\star} [M_{\odot} \text{Mpc}^{-3}]$		$z = 0$	$z = 1$	$z = 2$	$z = 5$
<b>MI</b>	$R < 0.5$	$7.73 \pm 0.13$	$7.64 \pm 0.16$	$7.46 \pm 0.19$	$7.01 \pm 0.43$
	Galaxy	$8.18 \pm 0.25$	$7.99 \pm 0.19$	$7.78 \pm 0.24$	$7.24 \pm 0.46$
	$1 < R < 2$	$7.70 \pm 0.26$	$7.37 \pm 0.13$	$7.10 \pm 0.18$	$6.47 \pm 0.34$
Driver et al.		8.30	8.08	7.90	7.70
Madau & Dickinson		8.56	8.32	8.01	5.92
$\log \rho_{\star} [M_{\odot} \text{Mpc}^{-3}]$		$z = 0$	$z = 1$	$z = 2$	$z = 5$
<b>MI</b>	$R < 0.5$	$8.02 \pm 0.13$	$7.87 \pm 0.16$	$7.66 \pm 0.19$	$7.14 \pm 0.42$
	Galaxy	$8.47 \pm 0.24$	$8.21 \pm 0.18$	$7.97 \pm 0.25$	$7.35 \pm 0.44$
	$1 < R < 2$	$7.99 \pm 0.25$	$7.58 \pm 0.14$	$7.29 \pm 0.18$	$6.60 \pm 0.34$

**Table 2.**  $\rho_{\text{SFR}}$ , sSFR, and  $\rho_{\star}$  for redshifts  $z = 0, 1, 2, 5$  obtained in this work. Results from Driver et al. (2017), Madau & Dickinson (2014), Fardal et al. (2007), and Elbaz et al. (2011) are included. The result from Driver et al. (2017) included in column  $z = 5$  in this table was measured, in fact, at a lookback time of 12.2 Gyr.

method to trace the evolution of these properties with respect to snapshots surveys of galaxy evolution obtained by studies at different redshifts. 2) To discuss the capability of a delayed- $\tau$  model, with respect to other parameterizations of the SFH, to trace the evolution of the star formation rate of the Universe.

### 5.1. The cosmic star formation rate density

One of the fundamental results obtained over the last two decades of observations from multiwavelength galaxy surveys is that the star formation rate density of the Universe peaked approximately 3.5 Gyr after the Big Bang, at  $z \sim 2$ , and declined thereafter (Lilly et al. 1996; Madau et al. 1998; Hopkins & Beacom 2006; Fardal et al. 2007; Madau & Dickinson 2014). Here, we extrapolate the SFR computed at each cosmic epoch from the CALIFA galaxies to derive the cosmic evolution of the SFR density ( $\rho_{\text{SFR}}$ ) and how it breaks up into contributions from current inner and outer galaxy regions, and into the different Hubble types.



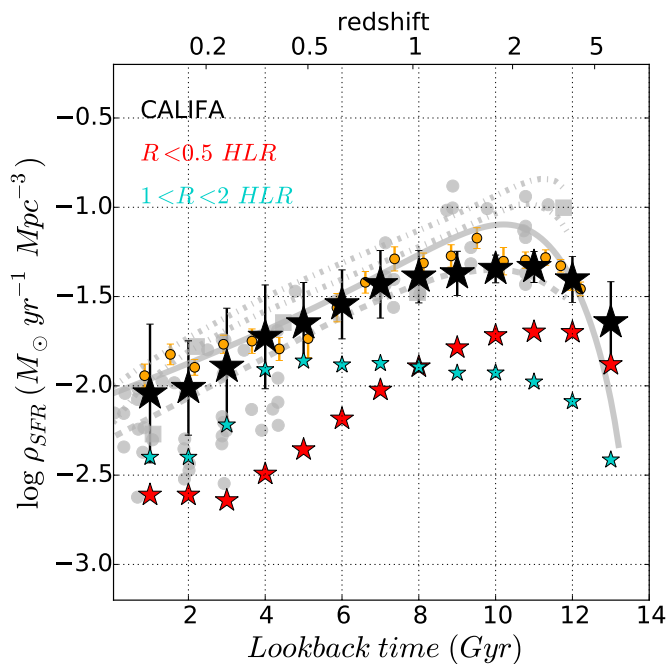


**Fig. 6.** The cosmic evolution of the star formation rate density,  $\rho_{\text{SFR}}$ , in the present study (black stars). Blue and red stars represent the contribution to  $\rho_{\text{SFR}}$  of the regions between 1 and 2 HLR and within the inner 0.5 HLR, respectively. Other results are from recent determinations by Gunawardhana et al. (2013, 2015) and their compilation (gray points), and the redshift evolution of  $\rho_{\text{SFR}}$  from Hopkins & Beacom (2006) (the top two gray dotted lines are  $\pm 1\sigma$  of their relation); Madau & Dickinson (2014) (middle gray full line); Fardal et al. (2007) (bottom gray dashed line); from the fossil record method applied to SDSS data by Panter et al. (2003) (gray squares); and from the work of Driver et al. (2017) for GAMA/G10-COSMOS/3D-HST data (orange dots). When needed, literature values have been scaled to a Chabrier IMF.

CALIFA, as many other samples, is not volume-limited, but it can be volume-corrected using the  $V_{\text{max}}$  method of Schmidt (1968). The volume available per galaxy,  $V_{\text{max}}$ , was calculated for the CALIFA mother sample assuming that the ratio between apparent and linear isophotal size of a galaxy depends only on its angular diameter distance (Walcher et al. 2014). In González Delgado et al. (2016), we used this method to derive a SFR density in the local Universe  $\rho_{\text{SFR}} = (0.0105 \pm 0.0008) M_{\odot} \text{ yr}^{-1} \text{ Mpc}^{-3}$  (for a Salpeter IMF), in very good agreement with independent estimates. Furthermore, we showed that most of the current star formation occurs in the disk of spirals. Now we extend this study by calculating  $\rho_{\text{SFR}}$  at different cosmic epochs using the 366 galaxies that belong to the CALIFA mother sample. We transform our  $\text{SFR}(t)$  estimates into  $\rho_{\text{SFR}}(t)$  by adding  $\text{SFR}(t)/V_{\text{max}}$  at each epoch and correcting the result by the fraction 937/366 to emulate what would be obtained for the full CALIFA mother sample of 937 galaxies.

Figure 6 places our values (black stars) in the  $\rho_{\text{SFR}}$  vs. lookbacktime (or redshift) diagram. The calculations are done at 1 Gyr time step, and the error in each epoch is obtained by propagating the dispersion of  $t_0$  and  $\tau$  of each galaxy.  $\rho_{\text{SFR}}$  shows a clear increase from  $z = 0$  to 1, a plateau between  $z = 1$  and 3, and a decrease at higher redshift.

Figure 6 includes (grey lines) the evolution of  $\rho_{\text{SFR}}$  from Madau & Dickinson (2014), Hopkins & Beacom (2006), and Fardal et al. (2007). It also includes  $\rho_{\text{SFR}}$  from the compilation of Gunawardhana et al. (2015, 2013), and the results obtained

by Panter et al. (2003) from the fossil record method applied to SDSS data (grey dots and squares). When necessary, the literature results are scaled to a Chabrier IMF. Our estimations are similar to the values from Fardal et al. (2007), but higher by 0.24 dex at  $z \sim 0$  (see also Table 2). In contrast, our  $\rho_{\text{SFR}}$  at  $z = 0$  is in agreement with Madau & Dickinson (2014) when their values are scaled by the change of IMF (Salpeter in Madau & Dickinson 2014 and Chabrier in this work); but it is below by 0.24 dex at  $z = 2$ .

Our results are also in excellent agreement with those obtained by Driver et al. (2017) using GAMA/G10-COSMOS/3D-HST data (orange points in Fig. 6). Their analysis (which takes in account the effects of dust, AGN, and cosmic variance) results in a plateau in  $\rho_{\text{SFR}}$  between  $z = 3$  and 1, similar to that found in our analysis. At  $z \sim 2$ , our results and those from Driver et al. (2017) are a factor 1.7 below the results from Bourne et al. (2017). This latter study reports that obscured star formation dominates the total  $\rho_{\text{SFR}}$  in massive galaxies at all redshifts, exceeding unobscured star formation by a factor  $> 10$ . We can think of three reasons for the discrepancy at  $z \sim 2$ : (i) The sample in Bourne et al. (2017) is dominated by dust obscured massive galaxies, and these may not be the progenitors of the CALIFA galaxies, which are representative of the current Hubble sequence. (ii) We cannot account for an extra dust obscuration at high redshift because our analysis does not assume a dust content evolution in the stellar populations. (iii) The Bourne et al. (2017) study is contaminated by AGN, which boost  $\rho_{\text{SFR}}$  at high redshift (as suggested by Driver et al. 2017).

On the whole, we conclude that our fossil-record estimates of  $\rho_{\text{SFR}}(t)$  are in good general agreement with the cosmological studies.

## 5.2. The cosmic specific star formation rate

In Sec. 4.5 and Fig. 5 we have presented our results on the evolution of the sSFR( $t$ ) as a function of Hubble type. Here, we discuss the average sSFR at each cosmic epoch, obtained weighting each galaxy by  $w_i = V_{\text{max},i}^{-1} / \sum_j V_{\text{max},j}^{-1}$ , where the sum runs over all galaxies. This volume weighted cosmic  $\langle \text{sSFR}(t) \rangle$  is shown as black stars in Fig. 7. As for  $\rho_{\text{SFR}}$ , the calculation is done in 1 Gyr intervals. In Table 2 we present the results for  $z = 0, 1, 2$ , and 5.

As expected,  $\langle \text{sSFR}(t) \rangle$  decreases with cosmic time. This result is in agreement with galaxy surveys at different redshifts. To illustrate this, Fig. 7 includes the evolution of sSFR( $t$ ) obtained by Madau & Dickinson (2014) (grey line), after scaling to a Chabrier IMF. It also includes results (grey dots and squares) from the compilation done by Lehnert et al. (2015) in their figure 2, based on measurements by Elbaz et al. (2007); Daddi et al. (2007); Dunne et al. (2009); Rodighiero et al. (2010); Oliver et al. (2010); Elbaz et al. (2011) in galaxy surveys at  $z \leq 2$ , and by Feulner et al. (2005); Stark et al. (2009); Magdis et al. (2010); Stark et al. (2013); Ilbert et al. (2013) at  $z \geq 2$ . Fig. 7 also shows (dark-grey line) the best-fit relation,  $\text{sSFR}(t) = 26 t^{2.2}$ , from Elbaz et al. (2011) over the range  $0 \leq z \leq 2$ , equivalent to  $\text{sSFR}(z) = (1 + z)^3 / t_{H_0}$ , where  $t_{H_0}$  is the Hubble time at  $z = 0$ . At  $z > 2$ , the cosmological galaxy surveys show that there is a plateau at  $2 \text{ Gyr}^{-1}$  that is in tension with the current galaxy-formation models (Weinmann et al. 2011). Several solutions have been proposed to bring into agreement models and observations. For example, to explain the sSFR plateau at  $z > 2$ , Lehnert et al. (2014) have argued that at these high redshifts the star formation must be self-regulated by high pressures, gener-

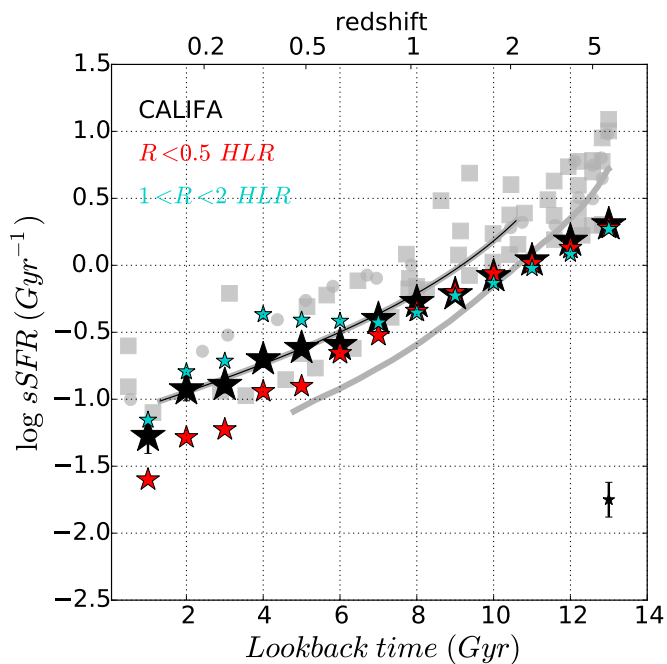


**Fig. 7.** The cosmic evolution of the  $sSFR(t)$  in the present study (black stars). The grey line is from Madau & Dickinson (2014), the dark-grey line is the  $(1+z)^3$  relation for  $z < 2$  from Elbaz et al. (2007), and grey symbols are from a compilation by Lehnert et al. (2015). Red and blue stars show the  $sSFR(t)$  corresponding to regions at the present epoch located at  $R < 0.5$  HLR and  $1 < R < 2$  HLR. The bars are the error in the mean, computed as the r.m.s. of the  $sSFR(t)$  values at each epoch divided by the square root of the number of galaxies in each bin

ated by the intense star formation itself, and it is the increase of the angular momentum with cosmic time what causes a decrease in the surface density of the accreted gas, and a decrease of  $sSFR$  as the Universe evolves.

Our results are in good agreement with cosmological surveys, and they follow well the time evolution curve for  $z < 1$  proposed by Elbaz et al. (2011). Although our value at  $z = 0$  is  $\sim 0.26$  dex below the Elbaz et al. (2011) curve, it is compatible with the lower envelope of individual values from the Lehnert et al. (2014) compilation, and above the Madau & Dickinson (2014) curve. At  $z = 1$ , we derive  $\langle sSFR(t) \rangle = 0.55 \text{ Gyr}^{-1}$ , just 10% smaller than in Elbaz et al. (2011). At  $1 < z < 2$  our values are below those from the fit estimated by Elbaz et al. (2011). But at  $z > 2$  our  $\langle sSFR(t) \rangle$  is compatible with the lower envelope of the observed galaxy surveys at  $z > 2$ ; e.g.  $\langle sSFR(t) \rangle = 0.74$ , and 1.44, for  $z = 2$  and 5, respectively.

### 5.3. The evolution of the cosmic stellar mass density

The stellar mass density,  $\rho_*$ , is also a relevant observational indicator of the physical processes that regulate the mass assembly in galaxies across cosmic time. Surveys, and in particular those done at near-infrared wavelengths, have provided important information about the stellar mass function at redshifts  $z > 2$  (e.g. Dickinson et al. 2003; Fontana et al. 2003; Rudnick et al. 2003). Others that combine observations at different wavelengths were able to study the time evolution of the mass function at high and intermediate redshifts (e.g. Muzzin et al. 2013; Ilbert et al. 2013; Moustakas & Metcalf 2003). One important conclusion

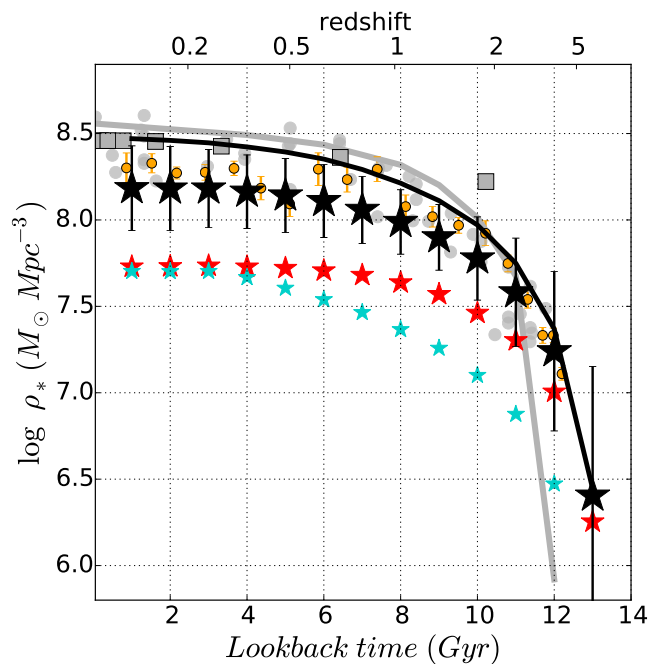


**Fig. 8.** The cosmic evolution of the stellar mass volume density,  $\rho_*$  (black stars), obtained with  $M_*(t)$  (corrected by mass-loss);  $\rho'_*$  (black line) obtained with  $M'_*(t)$  (mass formed). Orange points are from the GAMA survey by Driver et al. (2017). The grey line is from Madau & Dickinson (2014), grey squares are from Panter et al. (2007), and grey dots are from different galaxy surveys as explained in the text. Blue and red stars represent the contribution to  $\rho_*$  from the galaxy outer regions,  $1 \leq R \leq 2$  HLR, and inner regions,  $R \leq 0.5$  HLR, respectively.

from these studies was that the mass function has evolved very little since  $z = 1$  (e.g. Pozzetti et al. 2010).

At low-redshift, the SDSS survey also provided relevant information about the stellar mass function (e.g. Baldry et al. 2008, 2012). It has been very useful to construct a distribution of the stellar mass as a function of age (Gallazzi et al. 2008) and to derive  $\rho_*$  at  $z = 0$ , as well as to derive the cosmic evolution of  $\rho_*(t)$  by using the fossil record of the stellar population (Panter et al. 2007).

In our analysis, as explained in Section 4.5, the mass locked in stars up to a lookback time  $t$  is easily obtained from the  $SFR(t)$  fits. The volume density  $\rho_*$  is then obtained from these  $M_*(t)$  functions just as  $SFR(t)$  was used to derive  $\rho_{SFR}$  in Section 5.2. Fig. 8 places our results in the  $\rho_*$  vs. lookback time (or redshift) diagram, where the black stars and black line are the cosmic stellar mass density with and without correction for mass loss, respectively. Errors are obtained by propagating the dispersion of  $t_0$  and  $\tau$  of each galaxy. In agreement with galaxy redshift surveys,  $\rho_*$  shows little evolution since  $z = 1$ , but a fast increase at higher  $z$ . As a reference, the 50% point is reached at  $\sim 9$  Gyr lookback time.

Figure 8 also includes (grey line) the evolution of  $\rho_*$  from Madau & Dickinson (2014), after scaling to a Chabrier IMF. It also includes (grey dots)  $\rho_*$  from the compilation of Madau & Dickinson (2014) (their figure 11 and Table 2) based on measurements at different redshifts by Gallazzi et al. (2008); Li & White (2009); Moustakas et al. (2013) for  $z < 1$ , Arnouts et al. (2007); Pérez-González et al. (2008); Kajisawa et al. (2009); Marchesini et al. (2009); Pozzetti et al. (2010); Reddy & Steidel (2009); Ilbert et al. (2013); Muzzin et al. (2013) for  $0.1 < z < 4$ , Caputi

et al. (2011); Yabe et al. (2009); González et al. (2011); Lee et al. (2012); Labbé et al. (2013) for  $3 \leq z \leq 5$ . The results obtained by Panter et al. (2003) from the fossil record method applied to SDSS data are included as grey squares. Orange points are the recent results from GAMA/G10-COSMOS/3D-HST by Driver et al. (2017). When necessary, the literature results are scaled to a Chabrier IMF. We note that  $\rho_*$  by Madau & Dickinson (2014) is on average  $\sim 0.2$  dex higher than most of the data reported in the literature for  $0 < z < 3$ .

Comparing our results to galaxy redshift surveys, we found: a) at the highest redshifts (13 and 12 Gyr ago),  $\rho_*$  is higher than in Madau & Dickinson (2014); b) but at  $z \leq 1$ , our  $\rho_*$  is below the Madau & Dickinson (2014) curve and in agreement with the lower envelope of the grey dots. Our  $\rho_*$  is in very good agreement with the recent results from GAMA/G10-COSMOS/3D-HST multi-wavelength study (Driver et al. 2017). In particular, for  $z > 2$ , our results follow better the Driver et al. (2017) points than the Madau & Dickinson (2014) results, because they do not show the sudden rapid increase of the Madau & Dickinson (2014) curve. Furthermore, our values for lookback time at 12 and 13 Gyr ( $1.7 \times 10^7$  and  $2.5 \times 10^6 M_\odot \text{Mpc}^{-3}$ , respectively) are also in good agreement with the results reported by Duncan et al. (2014), Grazian et al. (2015), and Song et al. (2016), which range from  $2 \times 10^7$  to  $3 \times 10^6 M_\odot \text{Mpc}^{-3}$ .

The volume density  $\rho'_*$  from  $M'_*(t)$  (mass formed in stars) has a similar behavior to  $\rho_*$ . The difference between  $\rho_*$  and  $\rho'_*$  measures the stellar mass formed in galaxies that is returned to the interstellar medium due to stellar evolution. At expected,  $\rho'_* > \rho_*$  by 0.22 dex ( $z = 1$ ) to 0.29 dex ( $z = 0$ ); this is because for most galaxies in the sample  $t_0 > 10$  Gyr, and according with SSP models by Bruzual & Charlot (2003), the stellar population needs only  $\sim 4$  Gyr to lose  $\sim 0.45$  of its original mass, for a Chabrier IMF. Reassuringly, Driver et al. (2017) compute  $\rho'_*$  by integrating  $\rho_{\text{SFR}}$ , and comparing with  $\rho_*$  they obtain a returned mass fraction of  $0.50 \pm 0.07$ .

#### 5.4. SFH of galaxies: fossil cosmology vs redshift galaxy surveys

So far we have shown the capability of the delayed- $\tau$  model and nearby galaxies to trace the cosmic evolution of SFR and sSFR of the Universe. This SFH has been proposed to be an accurate representation of SFH of galaxies on the main sequence (Speagle et al. 2014). Madau & Dickinson (2014) have proposed a consistent picture in which the star formation rate density peaks at 3.5 Gyr after the Big Bang and then declines exponentially with an e-folding time of 3.9 Gyr. Similarly to Speagle et al. (2014), Madau & Dickinson (2014) derived their model from the fit to the evolution of  $\rho_{\text{SFR}}$  that was obtained from compilations of SFR using different SFR indicators and galaxy surveys, from the nearby Universe to high redshift ( $z \sim 5$ ).

In our case, we have derived SFR( $t$ ) by assuming that the SFH of nearby galaxies is well represented by a delayed- $\tau$  SFH. This model is able to provide estimations of cosmic star formation rate density and evolution of the sSFR that are compatible with  $\rho_{\text{SFR}}$  and sSFR derived from galaxy surveys. However, other parametric and non-parametric SFHs are able to fit equally well the observational constrains (see Appendix) and provide, to a first approximation, good estimates of  $\rho_{\text{SFR}}$  and sSFR (e.g. González Delgado et al. 2016, 2017). Here, we discuss the similarities and differences between the different models by comparing the mass fractions,  $m(t)$ , obtained with different parametric and non-parametric SFH applied to the CALIFA sample and with the mass fraction derived by Madau & Dickinson (2014).

For each galaxy,  $m(t)$  is derived by dividing the stellar mass formed in each epoch by the total mass formed up to that time. Previously in González Delgado et al. (2017), using a non-parametric method to derive the SFHs of CALIFA galaxies, we obtained that the highest mass fractions invariably occur at the earliest times. Subsequent star formation varies systematically with  $M_*$ , with the low  $M_*$  galaxies forming stars over extended periods of time, and high  $M_*$  galaxies exhibiting the fastest decline in  $m(t)$ . The behavior with morphology mimics the behavior with  $M_*$ ; for all morphologies,  $m(t)$  peaks at the earliest epoch and subsequent star formation increases systematically. Here, with the parametric delayed- $\tau$  SFH, we confirm that independently of morphology,  $m(t)$  has a maximum at  $z \geq 2$ ,  $\sim 10$  Gyr ago, with a small shift of  $\lesssim -0.1$  dex for Sc and Sd galaxies.

In order to obtain a global representation of the SFH of all the galaxies and compare with the results of Madau & Dickinson (2014), the average  $m(t)$  is obtained by weighting the mass fraction from each galaxy with  $w_i = V_{\text{max},i}^{-1} / \sum_j V_{\text{max},j}^{-1}$ . Fig. 9 shows a comparison of our results to those of Madau & Dickinson (2014) (the histogram on their figure 11, and the exponential law that they proposed). From our CALIFA sample,  $m(t)$  is obtained for: a) delayed- $\tau$  model; b) a combination of two exponential SFR; and c) using the non-parametric SFH derived from the STARLIGHT code. In addition to the description of the method used to obtain (b) and (c) models, a comparison of other properties related to the mass assembly in galaxies is also given in the Appendix.

The result from the delayed- $\tau$  model is quite similar to the exponential model of Madau & Dickinson (2014), with the highest fraction peaking  $\sim 3.5$  Gyr after the Big Bang, followed by a nearly exponential decline. Notice that there are slightly larger fractions at lookback times between 2 and 7 Gyr ago. This behavior is somewhat different to that obtained using two exponential SFR laws; while the maximum of  $m(t)$  occurred early on, at  $\sim 8$  Gyr ago ( $z \sim 1$ ), there is a secondary epoch,  $\sim 5$  Gyr ago, where the fraction of mass assembled is relevant before decaying to the actual values, this is not seen by Madau & Dickinson (2014). For the STARLIGHT non-parametric results,  $m(t)$  has two peaks 11 and 7 Gyr ago, which cover the same period of time than the peak of the delayed- $\tau$  model; then,  $m(t)$  declines in a similar way as the Madau & Dickinson (2014) model. However,  $m(t)$  derived from STARLIGHT shows other peak at very recent times,  $\sim 1$  Gyr, connected to the rejuvenation epoch that late spirals experienced in the last 2 Gyr.

In González Delgado et al. (2017) we suggest that galaxies can grow in two different modes. For the early evolution of Sa-Sbc spirals and the entire evolution of E and SO, the logarithm of their mass fraction,  $\log m(t)$ , declines linearly with  $\log t$ , i.e., as an exponential mode in  $m(t)$  vs.  $\log t$ . For the late types (Sc-Sd) and low-mass galaxies,  $\log m(t)$  vs.  $\log t$  is almost constant. We suggested that the first mode could represent the transition between the formation of a thick and a thin disk. The thick disk is a self-regulated mode, where strong outflows and turbulence drive the high intensity of the star formation rate that occurs very early on in the evolution (Lehnert et al. 2015). The second mode can be associated to the formation of the thin disk that is regulated by secular processes; a phase driven by self-gravity and energy injection from the stellar population is not relevant for global regulation (Lehnert et al. 2015).

It is interesting to notice that these two modes are again reproduced here by STARLIGHT using different constrains and SSPs models. However, while the exponential mode is well derived by the parametric SFH (delayed- $\tau$  model, or the two exponential SFRs) and the exponential mode by Madau & Dickinson (2014), the second mode for galaxy growth (not so relevant in

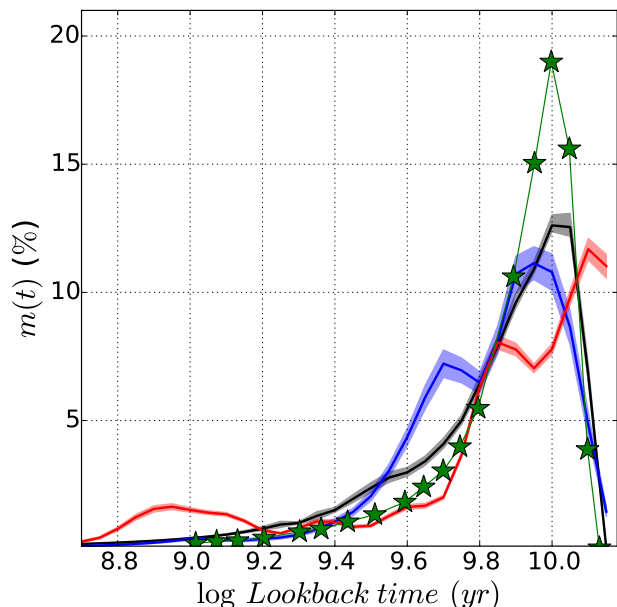


**Fig. 9.** Evolution of the mass fraction,  $m(t)$ , obtained with parametric SFHs: delayed- $\tau$  (black), a combination of two exponential SFR (blue), and STARLIGHT non-parametric (red), are compared with  $m(t)$  from Madau & Dickinson (2014) (green stars). The shaded bands around the mean curves represent  $\pm$  the error in the mean.

terms of the total mass assembled for most of the galaxies) is not reproduced by the delayed- $\tau$  model. This second mode of star formation is relevant in thin disks, the main contributors to  $\rho_{\text{SFR}}$  and sSFR at  $z = 0$  (González Delgado et al. 2016). This could explain why our delayed- $\tau$  model underestimates the sSFR at lookbacktime  $\lesssim 1$  Gyr.

## 6. Discussion: The cosmic evolution of the spatially-resolved SFR and stellar mass

Reassured by the satisfactory agreement between our estimates of  $\rho_{\text{SFR}}(t)$ , sSFR( $t$ ) and  $\rho_{\star}(t)$  and those obtained in galaxy surveys, we now go a step further and explore the spatially resolved and morphological information for our data set. The main goals of this section are to discuss: 1) The evolution of  $\rho_{\text{SFR}}$ , sSFR and  $\rho_{\star}$  separately for the inner and outer regions of galaxies. 2) The role of Hubble types in the budget of  $\rho_{\text{SFR}}$ , sSFR, and  $\rho_{\star}$ . 3) The evolution of the main sequence of star formation, and the comparison of the global relation with that obtained for the inner regions of galaxies.

### 6.1. The spatially-resolved evolution of $\rho_{\text{SFR}}$ , sSFR, and $\rho_{\star}$

Our data allow us to discuss the evolution of  $\rho_{\text{SFR}}$ , sSFR, and  $\rho_{\star}$  separately for the currently inner and outer regions of galaxies. This information is interesting because spatially-resolved spectroscopic observations of high redshift galaxies are difficult to obtain, and this analysis is an attempt to infer the contributions of different galaxy sub-components, bulge and disk, to the total budget of  $\rho_{\text{SFR}}$ , sSFR, and  $\rho_{\star}$ .

To evaluate the contribution of the different galaxy regions to  $\rho_{\text{SFR}}$ , we compute the contribution of zones located at  $R < 0.5$  HLR (“inner regions”, mainly dominated by the current bulge

component), and  $1 < R < 2$  HLR (“outer regions”, dominated by the disks). These contributions are plotted in Figs. 6, 7, and 8 as red and blue points, respectively, and they are listed in Table 2 for  $z = 0, 1, 2$ , and 5. The main results are:

- $\rho_{\text{SFR}}$  (Fig. 6): In the local Universe ( $z \sim 0$ ) the “disk” regions dominate  $\rho_{\text{SFR}}$  (González Delgado et al. 2016), while at higher redshift the main contributors are the inner regions. At  $z = 0$ , 27% of the  $\rho_{\text{SFR}}$  comes from the inner regions ( $R < 0.5$  HLR), while outer ones ( $1 < R < 2$  HLR) contribute with 44%. With redshift, the central contribution increases its relevance to the total SFR density, competing with the disk dominated regions at  $z \sim 1$ , where  $\rho_{\text{SFR}}(R < 0.5 \text{ HLR}) = \rho_{\text{SFR}}(1 < R < 2 \text{ HLR})$ , and dominating at higher  $z$ . These central regions contribute 51% of  $\rho_{\text{SFR}}$  at  $z \sim 5$ .
- sSFR( $t$ ) (Fig. 7): At  $z < 1$ , the outer galaxy regions have higher sSFR( $t$ ) than inner regions. This can be simply understood as a consequence of regions located in the disks being the major contributors to  $\rho_{\text{SFR}}$  at these redshifts. At higher  $z$ , regions located today in the inner 0.5 HLR (presumably associated to the present day bulge) and outwards of 1 HLR (belonging today to galaxy disks) have similar sSFR( $t$ ). These results suggest that all the regions are equally efficient in forming stars and growing their mass at high redshift.
- $\rho_{\star}$  (Fig. 8): In the local Universe ( $z < 0.2$ ), the outer and inner regions contribute to  $\rho_{\star}$  in very similar amounts. This agrees with our previous finding that the ratio of half mass to half light radii is close to unity (HMR/HLR  $\sim 0.8$  on average; González Delgado et al. (2014)). At higher redshifts the contribution from inner galaxy regions increases with respect to that from the outer zones by a factor 2.3 and 3.5 at  $z = 2$  and 5 (Table 2). Thus, the central regions of galaxies are the main place where  $\rho_{\star}$  was built. Comparing the blue and red stars it is clear that the central regions of galaxies have grown their mass more rapidly than the outer regions. Taking as reference the 50% point, for the central regions it was reached at lookback time 9 Gyr, and 6 Gyr ago for the outer regions. This conclusion is in agreement with our previous findings that galaxies grow their mass inside out (Pérez et al. 2013; García-Benito et al. 2017).

### 6.2. The role of morphology in the evolution of $\rho_{\text{SFR}}$ and $\rho_{\star}$

The Hubble sequence has evolved over time (Delgado-Serrano et al. 2010, e.g). In particular, early type galaxies (E, S0, and Sa) can be the end product of later type spirals transformed by mergers (e.g., Cappellari 2016 and references therein). Bearing in mind that our fossil record analysis cannot trace such morphological transformations, we now discuss the evolution of the SFR and stellar mass density as a function of the present day morphological type.

Previously, we have seen in González Delgado et al. (2016) that the local Universe ( $z = 0$ ), Sbc, Sc, and Sd galaxies dominate the  $\rho_{\text{SFR}}$  budget. We found that galaxies of these morphologies together they contribute  $\sim 66\%$  of  $\rho_{\text{SFR}}$ , while Sa and Sb galaxies contribute  $\sim 29\%$ . Here, we discuss the contribution of *currently* early (ETG; E, S0, and Sa), and late (LTG, Sb, Sbc, Sc, and Sd) type galaxies to the evolution of  $\rho_{\text{SFR}}$  and  $\rho_{\star}$ . Table 3 and Table 4 list their contributions, and Fig. 10 shows the results. A summary of the results are:

- $\rho_{\text{SFR}}$ : Present day ETG are the main contributors to  $\rho_{\text{SFR}}$ , except in the local universe (Fig. 10 top-left panel). At high



$\log \rho_{\text{SFR}} [M_{\odot}\text{yr}^{-1}\text{Mpc}^{-3}]$	$z = 0$	$z = 1$	$z = 2$	$z = 5$	
<b>M1</b>	$R < 0.5$	$-3.51 \pm 0.09$	$-2.07 \pm 0.10$	$-1.86 \pm 0.09$	$-1.81 \pm 0.06$
	ETG	$-2.94 \pm 0.15$	$-1.55 \pm 0.16$	$-1.52 \pm 0.09$	$-1.57 \pm 0.15$
	$1 < R < 2$	$-3.46 \pm 0.25$	$-2.18 \pm 0.42$	$-2.21 \pm 0.19$	$-2.37 \pm 0.23$
$\log \text{sSFR} [\text{Gyr}^{-1}]$	$R < 0.5$	$-2.77 \pm 0.01$	$-0.65 \pm 0.06$	$-0.48 \pm 0.04$	$-0.22 \pm 0.05$
<b>M1</b>	ETG	$-2.51 \pm 0.07$	$-0.55 \pm 0.12$	$-0.40 \pm 0.08$	$-0.16 \pm 0.07$
	$1 < R < 2$	$-2.38 \pm 0.02$	$-0.64 \pm 0.05$	$-0.49 \pm 0.06$	$-0.35 \pm 0.06$
$\log \rho_{\star} [M_{\odot}\text{Mpc}^{-3}]$	$R < 0.5$	$7.57 \pm 0.11$	$7.51 \pm 0.13$	$7.34 \pm 0.15$	$6.91 \pm 0.34$
<b>M1</b>	ETG	$8.00 \pm 0.26$	$7.82 \pm 0.22$	$7.61 \pm 0.28$	$7.08 \pm 0.51$
	$1 < R < 2$	$7.42 \pm 0.42$	$7.08 \pm 0.25$	$6.81 \pm 0.34$	$6.23 \pm 0.67$

**Table 3.**  $\rho_{\text{SFR}}$ , sSFR and  $\rho_{\star}$  for redshifts  $z = 0, 1, 2, 5$  obtained for early (E, S0, Sa) type galaxies.

$\log \rho_{\text{SFR}} [M_{\odot}\text{yr}^{-1}\text{Mpc}^{-3}]$	$z = 0$	$z = 1$	$z = 2$	$z = 5$	
<b>M1</b>	$R < 0.5$	$-2.72 \pm 0.12$	$-2.37 \pm 0.19$	$-2.27 \pm 0.07$	$-2.35 \pm 0.14$
	LTG	$-2.13 \pm 0.44$	$-1.95 \pm 0.12$	$-1.91 \pm 0.07$	$-2.00 \pm 0.12$
	$1 < R < 2$	$-2.46 \pm 0.07$	$-2.27 \pm 0.19$	$-2.36 \pm 0.09$	$-2.55 \pm 0.23$
$\log \text{sSFR} [\text{Gyr}^{-1}]$	$R < 0.5$	$-1.66 \pm 0.08$	$-0.64 \pm 0.04$	$-0.27 \pm 0.06$	$-0.13 \pm 0.06$
<b>M1</b>	LTG	$-1.31 \pm 0.20$	$-0.65 \pm 0.07$	$-0.37 \pm 0.06$	$-0.08 \pm 0.05$
	$1 < R < 2$	$-1.19 \pm 0.08$	$-0.67 \pm 0.03$	$-0.38 \pm 0.05$	$-0.12 \pm 0.05$
$\log \rho_{\star} [M_{\odot}\text{Mpc}^{-3}]$	$R < 0.5$	$7.20 \pm 0.11$	$7.05 \pm 0.16$	$6.83 \pm 0.22$	$6.28 \pm 0.41$
<b>M1</b>	LTG	$7.65 \pm 0.21$	$7.41 \pm 0.15$	$7.17 \pm 0.21$	$6.58 \pm 0.54$
	$1 < R < 2$	$7.29 \pm 0.42$	$6.93 \pm 0.15$	$6.65 \pm 0.24$	$5.95 \pm 0.61$

**Table 4.**  $\rho_{\text{SFR}}$ , sSFR and  $\rho_{\star}$  for redshifts  $z = 0, 1, 2, 5$  obtained for late (Sb, Sbc, Sc, Sd) type galaxies.

redshift, the progenitors of ETG dominate the SFR budget with  $\sim 69\%$  of  $\rho_{\text{SFR}}$ , while the progenitors of late type spirals contribute with  $\sim 26\%$ . However, at  $z = 0$ , LTG contribute with  $81\%$  of  $\rho_{\text{SFR}}$ , while current ETG contribute with less than  $12\%$  to the total  $\rho_{\text{SFR}}$ . The inner regions of the progenitors of present ETG contribute very little to the SFR density at the local universe ( $\sim 3\%$ ), but their contributions increase with redshift, with  $21\%$  at  $z = 1$  to  $40\%$  at  $z = 4$ . However, the inner regions of LTG contribute little to  $\rho_{\text{SFR}}$ , being  $\sim 11\%$  at any epoch, except at recent time, that contributes up to  $21\%$  of the total  $\rho_{\text{SFR}}(z = 0)$ . Furthermore, the outer regions of LTG are the major contributors to the SFR density at  $z = 0$ , at any other epoch, the outer regions of LTG or ETG contribute with  $\leq 16\%$  of the total budget  $\rho_{\text{SFR}}$ .

- sSFR( $t$ ): Except at low redshift, the sSFR evolves similarly for ETG and LTG. At  $z = 0$ , LTG have larger sSFR( $t$ ) than ETG. This is a consequence of their larger contribution to  $\rho_{\text{SFR}}$ . At higher redshifts the inner regions of ETG and LTG evolve in similar ways, and the same happens for the outer regions of ETG and LTG.
- $\rho_{\star}$ : At any epoch, the progenitors of present day ETG are the dominant population in terms of stellar mass (Fig. 10 bottom-left panel). They contribute to the total budget of  $\rho_{\star}$  by  $69\%$  at  $z = 5$  to  $66\%$  at  $z = 0$ ; but LTG contribute with  $< 30\%$  of the stellar mass density of the universe. The inner regions of ETG and their progenitors are also the main contributor to  $\rho_{\star}$ , going from  $25\%$  at  $z = 0$  to  $47\%$  at  $z = 5$ . The inner regions of LTG, however, contribute very little to the stellar mass density of the universe, being  $\sim 10\%$  of the total  $\rho_{\star}$  at any epoch. The outer regions of ETG or LTG contribute with  $\leq 17\%$  to the total budget of  $\rho_{\star}$ .

Thus, we can conclude that while in the local Universe the current SFR density is dominated by disks of LTG, at  $z > 1$  the SFR density is dominated by the central components of present day early type galaxies. Moreover, the inner regions of ETG are the major contributors to the total stellar mass density.

### 6.3. The evolution of the main sequence of star formation

Our analysis allows us to retrieve the correlation between SFR and  $M_{\star}$  at different redshifts, and to investigate the evolution of the slope and normalization of the MSSF. Furthermore, the effect of spatially-sampling in the MSSF. Studies have shown that the correlation found in the nearby Universe (Brinchmann et al. 2004; Salim et al. 2007; Renzini & Peng 2015; Catalán-Torrecilla et al. 2015b; González Delgado et al. 2016) persists up to  $z \sim 7$  (Noeske et al. 2007; Daddi et al. 2007; Pannella et al. 2009; Peng et al. 2010; Wuyts et al. 2011; Whitaker et al. 2012).

At  $z = 0$ , it is well proved that MSSF relation is sub-linear, although its slope varies depending on the galaxy sample selection and on the indicator used to estimate the SFR (Speagle et al. 2014). Observationally, there is also evidence that the slope and normalization of MSSF evolves with lookback time, although the role of the galaxy sample selection and the effect of extinction is not yet understood (Noeske et al. 2007; Elbaz et al. 2007; Salim et al. 2007; Schiminovich et al. 2007; Pannella et al. 2009; Whitaker et al. 2012). For example, by studying a large sample of star forming galaxies out to  $z = 2.5$  Whitaker et al. (2012) found that the slope of the relation decreases at higher redshifts as a consequence of the sample being more biased to dusty star forming galaxies. Moreover since, on average, star forming galaxies in the past had larger SFR than today (Madau & Dickinson 2014), it is expected that the MSSF changes with time, at least in the zero point. More recently, Speagle et al. (2014) have used a compilation of data from 25 different surveys from the literature and they analyze, in a highly consistent framework, the evolution of the slope and zero point of the MSSF relation from  $z = 0$  to  $z = 6$ . After accounting for the scatter between the different SFR indicators, they found that the slope and zero-point of the MSSF are likely time dependent. Thus, the slope (and zero-point) of the MSSF increases (decreases) with redshift and lookback time. In contrast, Lee et al. (2015) have found that the star forming galaxies in the COSMOS field at  $z \leq 1.3$  observed at far-infrared wavelengths follow a broken-law,  $\text{SFR} \propto M_{\star}^{0.88 \pm 0.06}$  below the turnover mass of  $10^{10}$ , and  $\text{SFR} \propto M_{\star}^{0.27 \pm 0.04}$  above  $10^{10}$ . Later, using data from the FourStar Galaxy Evolution Survey (ZFOURGE) at  $0.5 < z < 4$  Tomczak et al. (2016) found that the turnover mass ( $M_0$ ) can range from  $10^{9.5}$  to  $10^{10.8}$ , with evidence that  $M_0$  increases with redshift.

With a completely different approach to redshift surveys, our analysis allows us to investigate the evolution of MSSF and to compare with galaxy redshift surveys. Indeed, our results on SFR( $t$ ) presented in Section 4.3 and González Delgado et al. (2017) confirm that SFR( $t$ ) declines since  $z \lesssim 2$ , and  $M_{\star}(t)$  has grown little since  $z \lesssim 1$  (García-Benito et al. 2017; Pérez et al. 2013). Thus, we should expect that the MSSF at earlier epochs is shifted up with respect to the current MSSF. Furthermore, the decreasing scatter with increasing redshift can be understood because galaxies that today are out of the MSSF (because the star formation has been quenched) in the past could have been actively forming stars and be well placed on the MSSF.

Figure 11 (upper panel) presents our MSSF extracted at four redshifts:  $z = 0, 0.5, 1$ , and  $2$ . It also shows the relations found by fitting only current star forming Sc galaxies, and all the galaxies of the sample. The first result to notice is that, while at  $z = 0$  the relation fitted for Sc and all the galaxies are very different, mainly due to ETGs that are off down the MSSF, at higher redshift, the two fits are quite similar. Considering only Sc galaxies we obtain a slope,  $a = 0.66 \pm 0.17$ , and a zero-point,  $b = -6.55 \pm 0.09$ , at  $z = 0$ , and  $a = 0.91 \pm 0.04$  and  $b = -8.20 \pm 0.03$  at  $z = 2$ . If all the galaxies are included, the



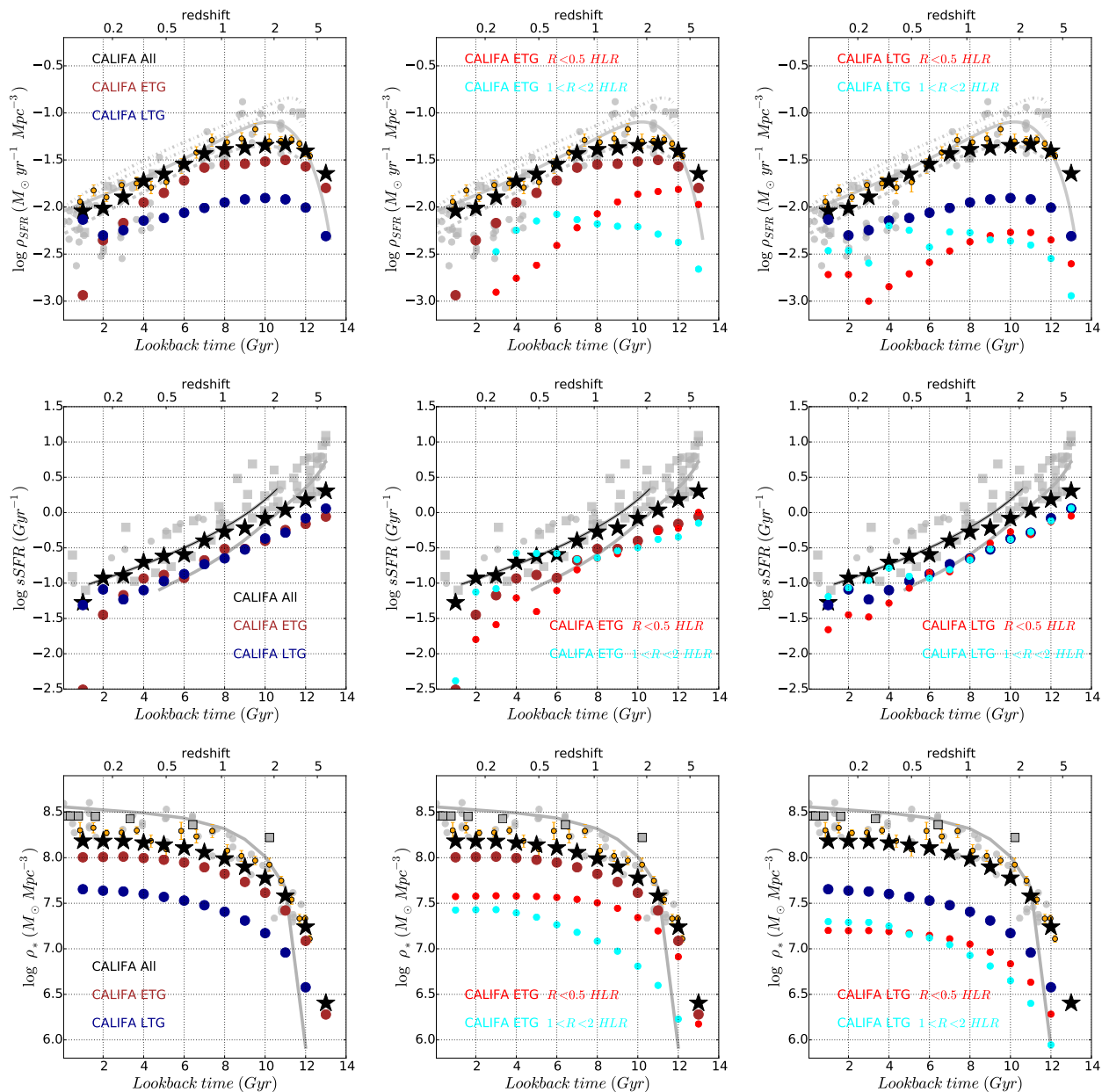


**Fig. 10.** The cosmic evolution of the star formation rate density,  $\rho_{\text{SFR}}$  (upper panels), the sSFR(t) (middle panels), and the stellar mass volume density,  $\rho_*$  (lower panels), as a function of the morphology: early (E-S0-Sa) and late (Sb-Sbc-Sc-Sd) type galaxies. The contribution of inner ( $R < 0.5$  HLR) and outer ( $1 < R < 2$  HLR) regions of ETG and LTG are in the central and right panels, respectively.

slope (zero-point) also increases (decreases) significantly with redshift (see Table 5).

There are several other interesting results: a) the scatter in the MSSF decreases significantly with redshift. The progenitors of all the galaxies in the sample were in the MSSF at  $z \geq 2$ ; b) the progenitors of E and S0 were in or above the MSSF at  $z = 1$ .

Our results are in agreement with those of Speagle et al. (2014) and Chiosi et al. (2017), in the sense that the MSSF slope is time dependent and flattens from high to low redshift. However, this slope does not decrease linearly with the age of the Universe, because our data show relatively little change from  $z = 2$  to  $z = 1$ . The flattening from  $z = 1$  to 0, though, is equal to their prediction.

Figure 11 also shows (purple line) the results for the MSSF by the *Illustris* cosmological hydrodynamical simulation of galaxy formation (Nelson et al. 2015), and observational results

from a compilation by Behroozi et al. (2013) that we took from figure 1 in Sparre et al. (2015). The results for  $z = 0.5$  are taken from the *Illustris* simulation at  $0.5 < z < 1$  as presented in figure 6 in Tomczak et al. (2016). Fig. 11 shows that the *Illustris* simulation at  $z = 1$  and 2 follow very well our results, as well as the trend of galaxies going out from the main sequence at  $z \leq 0.5$ . At any redshift, the points from the compilation by Behroozi et al. (2013) have a flatter slope than our results and the *Illustris* simulation, and at  $z = 1, 2$ , they are above the MSSF traced by *Illustris* and our MSSF fit. However these points are located in a region populated by the progenitors of current ETG (E, S0, Sa) that were above the MSSF at  $z = 1, 2$ .

Other high redshift galaxy surveys have also shown that passive galaxies do exist up to at least  $z \sim 2$ , in particular at high masses (e.g. Cimatti et al. 2004, Glazebrook et al. 2004), that the red sequence of galaxies was present at  $z \approx 1$  (e.g. Wuyts et al.

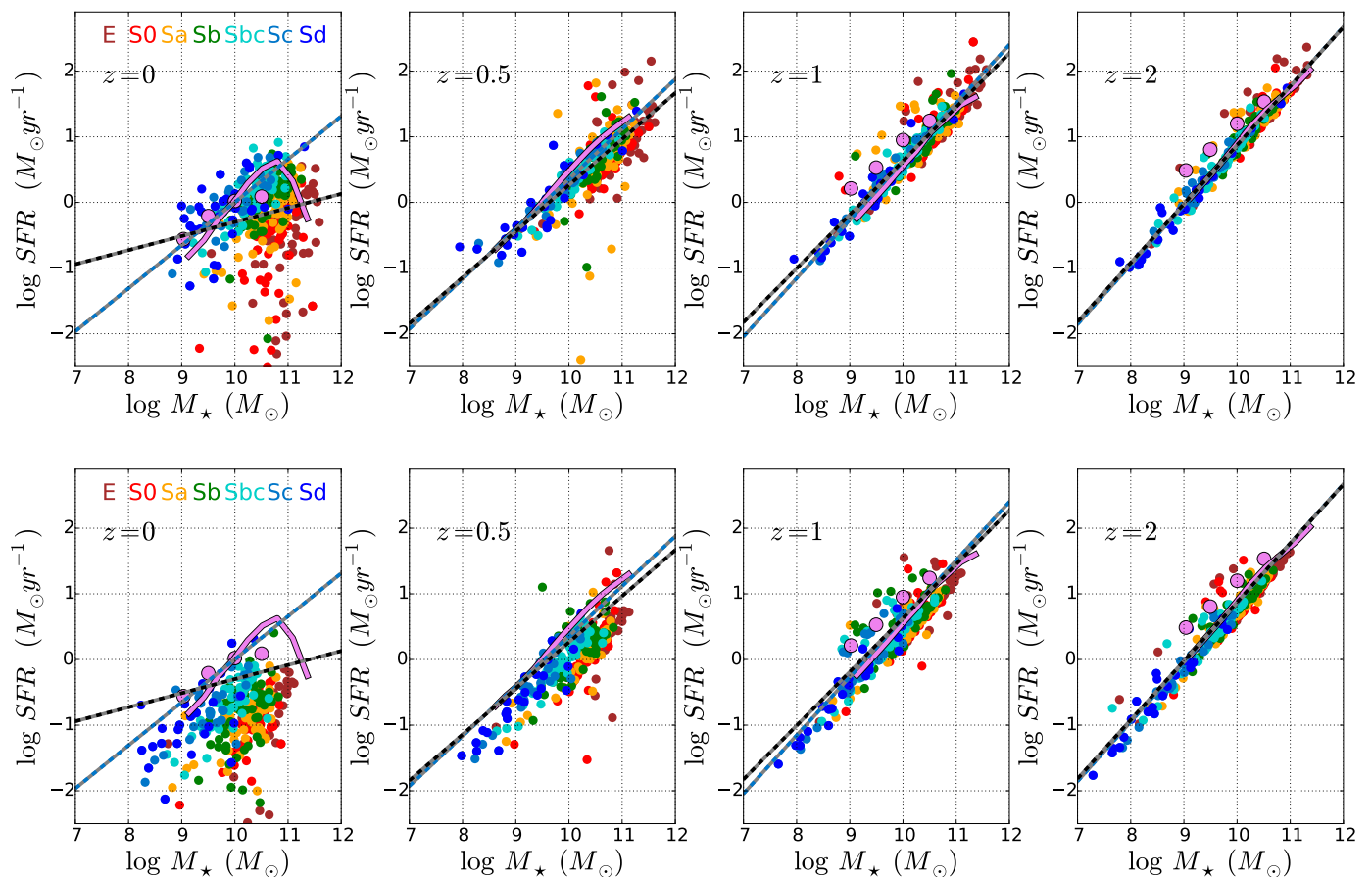


**Fig. 11.** Upper panels: The evolution of MSSF from  $z=2$  (right panel) to  $z=0$  (left panel). Galaxies are color coded according with the morphology. The blue line is a linear fit to Sc galaxies. The black line is a fit to all galaxies. Lower panels: as in the upper panels but using only the contributions to SFR and  $M_*$  of the galaxies current inner regions ( $R \leq 0.5$  HLR). Blue-gray and black-gray lines (in upper and lower panels) are fits to  $\log \text{SFR} - \log M_*$  for Sc and for all the galaxies in this study. Big purple dots are from the compilation by Behroozi et al. (2013), and the purple line is the MSSF from the *Illustris* simulation by Sparre et al. (2015) and Tomczak et al. (2016).

2011). However, Fig. 11 (upper panels) shows that current ETGs are not out of the MSSF until relatively recent,  $z \leq 0.5$ . To check how this result depends on the spatial sampling, we obtain the  $\text{SFR}^{\text{in}}(t)$  and  $M_*^{\text{in}}(t)$  for the galaxy regions that today are located in the central 0.5 HLR (lower panels). The lines are the same as in the upper panels. We found that at  $z \geq 1$ , the inner regions were still on the MSSF, and it is at lower redshift that these regions migrate off the MSSF. Thus, our results suggest that the massive passive and dead galaxies detected at  $z \geq 2$  by high redshift galaxy surveys cannot be the progenitors of current ETGs in the CALIFA survey. Spectroscopically confirmed quiescent galaxies at  $z > 2$  have masses already in excess of  $\log M_* \sim 10.5 - 11$  (e.g. Toft et al. 2012; Belli et al. 2017); thus, if they further grow through mergers, their descendants may be more massive galaxies not sampled in the CALIFA volume.

Overall, our results point to the idea that the MSSF could be a natural consequence of the cold mode accretion of galaxies (Birnboim & Dekel 2003), where the supply of gas feeding the star formation in galaxies follows the dark matter halo accretion rate, with coupled baryons and dark matter halo. However, because the slope is  $< 1$  even at very high redshift, feedback may also play a role in making the relation sub-linear.

	$ax+b$	$z=0$	$z=0.5$	$z=1$	$z=2$
Sc	$a$	$0.66 \pm 0.17$	$0.76 \pm 0.09$	$0.89 \pm 0.05$	$0.91 \pm 0.04$
	$b$	$-6.55 \pm 0.09$	$-7.25 \pm 0.05$	$-8.27 \pm 0.04$	$-8.20 \pm 0.03$
All galaxies	$a$	$0.21 \pm 0.05$	$0.70 \pm 0.03$	$0.82 \pm 0.02$	$0.90 \pm 0.01$
	$b$	$-2.44 \pm 0.03$	$-6.76 \pm 0.03$	$-7.56 \pm 0.02$	$-8.09 \pm 0.02$

**Table 5.** Parameters of  $\log \text{SFR} (M_\odot \text{ yr}^{-1}) = a \log M_* (M_\odot) + b$  fits of the MSSF at different redshifts obtained for Sc and all the galaxies.

## 7. Summary and conclusions

Using the stellar populations fossil record method for a sample of 366 CALIFA galaxies with GALEX images, we obtained the cosmic evolution of the absolute and specific star formation rate in galaxies, and galaxy mass. These properties were estimated for galaxies with stellar mass in the range  $\sim 10^9$  to  $10^{12}$  (for a Chabrier IMF), stacking the results as a function of Hubble type (E, S0, Sa, Sb, Sbc, Sc and Sd). A bayesian method based on parametric SFHs that fits simultaneously the FUV, NUV, and u,g,r,i,z-bands, and the  $D_n4000$ ,  $H\beta$ , and  $[\text{MgFe}]'$  indices from the data cubes is also presented. In the main body of the paper, we discuss the results obtained by using a parametric delayed- $\tau$  SFH. In the appendix, the results obtained with other parameterizations (formed by a single or by a combination of two laws) are compared with the delayed- $\tau$  model. Furthermore, we compare these results with those obtained by fitting the UV band

and the full CALIFA spectra using a recent version of the non-parametric code *STARLIGHT* (López Fernández et al. 2016). The fits are processed to derive the time evolution of  $SFR(t)$ , and  $sSFR(t)$  for three different regions in each galaxy at the present epoch: a) 0–2 HLR, b) 0–0.5 HLR, c) 1–2 HLR, as representative of the "whole" (integrated) galaxy, the innermost regions (dominated in most of the galaxies by the spheroidal or bulge component), and outer regions (dominated by the disk in spirals).

Our main results are:

- At any epoch, the SFR scales with the current Hubble type, as expected from the dependence of SFR with  $M_*$ , and of galaxy mass with morphology. The highest SFR ( $\sim 40 M_\odot \text{ yr}^{-1}$ ) occurred in E galaxies at  $z \sim 1 - 2$ . The lowest SFR at similar epochs occurs in late spirals Sd ( $\sim 3 M_\odot \text{ yr}^{-1}$ ). SFR in the inner regions of E peak at  $z \sim 2$ , while it peaks at  $z < 1$  in the outer regions. The SFR peak in early spirals (Sa, Sb, Sbc) occurred earlier than in E and S0. The SFR peak in the inner regions occurred at a similar epoch in E, S0, and early spirals; earlier than for late type spirals.
- These results are a consequence of the values obtained for the parameters  $t_0$  and  $\tau$ . For Sa-Sbc  $t_0 \sim 12$  Gyr,  $t_0 \sim 10$  Gyr for E and S0, and  $t_0 \sim 10 - 9$  Gyr in Sc and Sd galaxies. For the present inner regions,  $t_0 - \tau$  is larger than that of the whole galaxy and of the present outer regions, indicating that the inner regions formed earlier than outer ones, and that galaxies formed inside-out. The e-folding time,  $\tau$  increases with morphological type, and is higher in the outer than in the inner regions of spirals, indicating that star formation is more extended in time in late than in early type spirals.
- The CALIFA sample is well suited to compute the evolution of  $\rho_{SFR}$  and  $\rho_*$  which is in agreement with results obtained from galaxy surveys, in particular with the recent estimations obtained from GAMA + G10-COSMOS/3D-HST by Driver et al. (2017). At  $z \leq 0.5$  the majority of  $\rho_{SFR}$  takes place in the outer regions of galaxies, but at higher redshifts the present inner regions ( $< 0.5$  HLR) play a major role in building  $\rho_{SFR}$  and  $\rho_*$  dominating at  $z > 2$ . In terms of morphology, while at  $z = 0$  late spirals dominate the  $\rho_{SFR}$  budget, at  $z > 2$  the progenitors of the present E and S0 are the major contributors to the SFR density and  $\rho_*$ . Taken as reference the 50% point of  $\rho_*$ , the inner regions reached this value at 9 Gyr lookback time, and the outer regions at 6 Gyr. This delay between the inner and outer regions confirms that galaxies grow inside-out.
- The  $sSFR$  declines rapidly as the Universe evolves, although the slope depends on the morphology, steeper for early than for late type galaxies. In the inner regions,  $sSFR$  declines with time more rapidly than in the outer regions in early spirals (Sa-Sbc) and E and S0, suggesting an earlier epoch for the shut down of the star formation.
- The MSSF is traced up to  $z > 2$ . We find that the slope evolves with time, in agreement with cosmological galaxy surveys. The slope flattens from  $0.9 \pm 0.01$  at  $z = 2$  to  $0.66 \pm 0.17$  at the present epoch (when only Sc galaxies are considered). Our estimations of the evolution of the MSSF are in good agreement with the predictions by the *Illustris* simulation. They suggest that the MSSF is a natural consequence of a cold mode accretion, although feedback may also play some role to set the slope of the correlation below to 1.
- The comparison of nine different parametric SFHs (described in the Appendix) indicates that a delayed- $\tau$  SFR is

the model that provides better match between our results and those from the snapshots of galaxy evolution obtained by studies at different redshifts for  $\rho_{SFR}$ ,  $sSFR(t)$ , and  $\rho_*$ . The average SFH of galaxies, as represented by  $m(t)$  vs lookback time of CALIFA galaxies, confirms that globally galaxies grow their mass mainly in a mode that is well represented by a delayed- $\tau$ , where the maximum peaks at high redshift ( $z \sim 2$ ), and then declines exponentially with an e-folding time of  $\sim 3.9$  Gyr. This result is in agreement with the model proposed by Madau & Dickinson (2014) and our previous results using non-parametric SFH (González Delgado et al. 2017).

These results show again the uniqueness of the CALIFA survey to characterize the the cosmic evolution of the spatially-resolved SFR and stellar mass of galaxies. The fossil record of the stellar populations of this sample of nearby galaxies has been very successful to derive  $\rho_{SFR}$ ,  $sSFR$ , and  $\rho_*$ , that are in good agreement with the results from the snapshot galaxy surveys in a large range of redshifts. Thanks to the spatially-resolved data, we have retrieved the contributions of different regions of early type and spirals to  $\rho_{SFR}$ , and  $\rho_*$ .

*Acknowledgements.* CALIFA is the first legacy survey carried out at Calar Alto. The CALIFA collaboration would like to thank the IAA-CSIC and MPIA-MPG as major partners of the observatory, and CAHA itself, for the unique access to telescope time and support in manpower and infrastructures. We also thank the CAHA staff for the dedication to this project. Support from the Spanish Ministerio de Economía y Competitividad, through projects AYA2016-77846-P, AYA2014-57490-P, AYA2010-15081, and Junta de Andalucía FQ1580. We also thank the Viabilidad, Diseño, Acceso y Mejora funding program, ICTS-2009-10, for funding the data acquisition of this project. RCF thanks the hospitality of the IAA and the support of CNPq. RGD acknowledges the support of CNPq (Brazil) through Programa Ciência sem Fronteiras (401452/2012-3). RCF and NVA acknowledge the support from the CAPES C&F-PVE project 88881.068116/2014-01. SFS thanks the ConaCyt programs IA-180125 and DGAPA IA101217 for their support to this project. We thank the support of the IAA Computing group, and to the referee for useful comments.

## References

- Ahn, C. P., Alexandroff, R., Allende Prieto, C., et al. 2014, *ApJS*, 211, 17
- Alongi, M., Bertelli, G., Bressan, A., et al. 1993, *A&AS*, 97, 851
- Arnouts, S., Walcher, C. J., Le Fèvre, O., et al. 2007, *A&A*, 476, 137
- Asari, N. V., Cid Fernandes, R., Stasińska, G., et al. 2007, *MNRAS*, 381, 263
- Baldry, I. K., Driver, S. P., Loveday, J., et al. 2012, *MNRAS*, 421, 621
- Baldry, I. K., Glazebrook, K., & Driver, S. P. 2008, *MNRAS*, 388, 945
- Baldry, I. K., Robotham, A. S. G., Hill, D. T., et al. 2010, *MNRAS*, 404, 86
- Balogh, M. L., Morris, S. L., Yee, H. K. C., Carlberg, R. G., & Ellingson, E. 1999, *ApJ*, 527, 54
- Behroozi, P. S., Wechsler, R. H., & Conroy, C. 2013, *ApJ*, 770, 57
- Belli, S., Genzel, R., Förster Schreiber, N. M., et al. 2017, *ApJ*, 841, L6
- Birnboim, Y. & Dekel, A. 2003, *MNRAS*, 345, 349
- Birnboim, Y., Dekel, A., & Neistein, E. 2007, *MNRAS*, 380, 339
- Blanton, M. R. & Moustakas, J. 2009, *ARA&A*, 47, 159
- Bluck, A. F. L., Conselice, C. J., Bouwens, R. J., et al. 2009, *MNRAS*, 394, L51
- Bluck, A. F. L., Conselice, C. J., Buitrago, F., et al. 2012, *ApJ*, 747, 34
- Bourne, N., Dunlop, J. S., Merlin, E., et al. 2017, *MNRAS*, 467, 1360
- Bressan, A., Fagotto, F., Bertelli, G., & Chiosi, C. 1993, *A&AS*, 100, 647
- Brinchmann, J., Charlot, S., White, S. D. M., et al. 2004, *MNRAS*, 351, 1151
- Bruzual, G. & Charlot, S. 2003, *MNRAS*, 344, 1000
- Bruzual A., G. & Kron, R. G. 1980, *ApJ*, 241, 25
- Bryant, J. J., Owers, M. S., Robotham, A. S. G., et al. 2015, *MNRAS*, 447, 2857
- Bundy, K., Bershady, M. A., Law, D. R., et al. 2015, *ApJ*, 798, 7
- Bundy, K., Fukugita, M., Ellis, R. S., et al. 2009, *ApJ*, 697, 1369
- Calzetti, D., Armus, L., Bohlin, R. C., et al. 2000, *ApJ*, 533, 682
- Cano-Díaz, M., Sánchez, S. F., Zibetti, S., et al. 2016, *ApJ*, 821, L26
- Cappellari, M. 2016, *ARA&A*, 54, 597
- Cappellari, M., Emsellem, E., Krajnović, D., et al. 2011, *MNRAS*, 413, 813
- Caputi, K. I., Cirasuolo, M., Dunlop, J. S., et al. 2011, *MNRAS*, 413, 162
- Casteels, K. R. V., Conselice, C. J., Bamford, S. P., et al. 2014, *MNRAS*, 445, 1157

- Catalán-Torrecilla, C., Gil de Paz, A., Castillo-Morales, A., et al. 2015a, *A&A*, 584, A87
- Catalán-Torrecilla, C., Gil de Paz, A., Castillo-Morales, A., et al. 2015b, *A&A*, 584, A87
- Catalán-Torrecilla, C., Gil de Paz, A., Castillo-Morales, A., et al. 2017, *ApJ*, 848, 87
- Chabrier, G. 2003, *PASP*, 115, 763
- Chiosi, C. 1980, *A&A*, 83, 206
- Chiosi, C., Sciaratta, M., D’Onofrio, M., et al. 2017, *ArXiv e-prints*
- Cid Fernandes, R., González Delgado, R. M., García Benito, R., et al. 2014, *A&A*, 561, A130
- Cid Fernandes, R., Mateus, A., Sodré, L., Stasińska, G., & Gomes, J. M. 2005, *MNRAS*, 358, 363
- Cid Fernandes, R., Pérez, E., García Benito, R., et al. 2013, *A&A*, 557, A86
- Cimatti, A., Daddi, E., Renzini, A., et al. 2004, *Nature*, 430, 184
- Citro, A., Pozzetti, L., Moresco, M., & Cimatti, A. 2016, *A&A*, 592, A19
- Cortijo-Ferrero, C., González Delgado, R. M., Pérez, E., et al. 2017, *ArXiv e-prints*
- Daddi, E., Dickinson, M., Morrison, G., et al. 2007, *ApJ*, 670, 156
- de Amorim, A. L., García-Benito, R., Cid Fernandes, R., et al. 2017, *MNRAS*, 471, 3727
- Dekel, A., Birnboim, Y., Engel, G., et al. 2009a, *Nature*, 457, 451
- Dekel, A., Sari, R., & Ceverino, D. 2009b, *ApJ*, 703, 785
- Delgado-Serrano, R., Hammer, F., Yang, Y. B., et al. 2010, *A&A*, 509, A78
- Dickinson, M., Papovich, C., Ferguson, H. C., & Budavári, T. 2003, *ApJ*, 587, 25
- Driver, S. P., Andrews, S. K., da Cunha, E., et al. 2017, *ArXiv e-prints*
- Duncan, K., Conselice, C. J., Mortlock, A., et al. 2014, *MNRAS*, 444, 2960
- Dunne, L., Ivison, R. J., Maddox, S., et al. 2009, *MNRAS*, 394, 3
- Dutton, A. A., van den Bosch, F. C., & Dekel, A. 2010, *MNRAS*, 405, 1690
- Elbaz, D., Daddi, E., Le Borgne, D., et al. 2007, *A&A*, 468, 33
- Elbaz, D., Dickinson, M., Hwang, H. S., et al. 2011, *A&A*, 533, A119
- Fagotto, F., Bressan, A., Bertelli, G., & Chiosi, C. 1994a, *A&AS*, 104, 365
- Fagotto, F., Bressan, A., Bertelli, G., & Chiosi, C. 1994b, *A&AS*, 105, 29
- Falcón-Barroso, J., Sánchez-Blázquez, P., Vazdekis, A., et al. 2011, *A&A*, 532, A95
- Fardal, M. A., Katz, N., Weinberg, D. H., & Davé, R. 2007, *MNRAS*, 379, 985
- Feulner, G., Gabasch, A., Salvato, M., et al. 2005, *ApJ*, 633, L9
- Fontana, A., Poli, F., Menci, N., et al. 2003, *ApJ*, 587, 544
- Gallagher, III, J. S., Hunter, D. A., & Tutukov, A. V. 1984, *ApJ*, 284, 544
- Gallazzi, A., Brinchmann, J., Charlot, S., & White, S. D. M. 2008, *MNRAS*, 383, 1439
- Gallazzi, A., Charlot, S., Brinchmann, J., & White, S. D. M. 2006, *MNRAS*, 370, 1106
- Gallego, J., Zamorano, J., Aragon-Salamanca, A., & Rego, M. 1995, *ApJ*, 455, L1
- García-Benito, R., González Delgado, R. M., Pérez, E., et al. 2017, *ArXiv e-prints*
- García-Benito, R., Zibetti, S., Sánchez, S. F., et al. 2015, *A&A*, 576, A135
- Gavazzi, G., Bonfanti, C., Sanvito, G., Boselli, A., & Scodreggio, M. 2002, *ApJ*, 576, 135
- Girardi, L., Bressan, A., Chiosi, C., Bertelli, G., & Nasi, E. 1996, *A&AS*, 117, 113
- Glazebrook, K., Abraham, R. G., McCarthy, P. J., et al. 2004, *Nature*, 430, 181
- Goddard, D., Thomas, D., Maraston, C., et al. 2016, *ArXiv e-prints*
- González, V., Labbé, I., Bouwens, R. J., et al. 2011, *ApJ*, 735, L34
- González Delgado, R. M., Cerviño, M., Martins, L. P., Leitherer, C., & Hauschildt, P. H. 2005, *MNRAS*, 357, 945
- González Delgado, R. M., Cid Fernandes, R., Pérez, E., et al. 2016, *A&A*, 590, A44
- González Delgado, R. M., García-Benito, R., Pérez, E., et al. 2015, *A&A*, 581, A103
- González Delgado, R. M., Pérez, E., Cid Fernandes, R., et al. 2014, *A&A*, 562, A47
- González Delgado, R. M., Pérez, E., Cid Fernandes, R., et al. 2017, *ArXiv e-prints*
- Grazian, A., Fontana, A., Santini, P., et al. 2015, *A&A*, 575, A96
- Gunawardhana, M. L. P., Hopkins, A. M., Bland-Hawthorn, J., et al. 2013, *MNRAS*, 433, 2764
- Gunawardhana, M. L. P., Hopkins, A. M., Taylor, E. N., et al. 2015, *MNRAS*, 447, 875
- Heavens, A., Panter, B., Jimenez, R., & Dunlop, J. 2004, *Nature*, 428, 625
- Hopkins, A. M. & Beacom, J. F. 2006, *ApJ*, 651, 142
- Husemann, B., Jahnke, K., Sánchez, S. F., et al. 2013, *A&A*, 549, A87
- Ibarra-Medel, H. J., Sánchez, S. F., Avila-Reese, V., et al. 2016, *MNRAS*, 463, 2799
- Ilbert, O., McCracken, H. J., Le Fèvre, O., et al. 2013, *A&A*, 556, A55
- Kajisawa, M., Ichikawa, T., Tanaka, I., et al. 2009, *ApJ*, 702, 1393
- Karim, A., Schinnerer, E., Martínez-Sansigre, A., et al. 2011, *ApJ*, 730, 61
- Kauffmann, G., Heckman, T. M., White, S. D. M., et al. 2003, *MNRAS*, 341, 54
- Kaviraj, S., Devriendt, J., Dubois, Y., et al. 2015, *MNRAS*, 452, 2845
- Kaviraj, S., Schawinski, K., Devriendt, J. E. G., et al. 2007, *ApJS*, 173, 619
- Kelz, A., Verheijen, M. A. W., Roth, M. M., et al. 2006, *PASP*, 118, 129
- Kereš, D., Katz, N., Weinberg, D. H., & Davé, R. 2005, *MNRAS*, 363, 2
- Koleva, M., Prugniel, P., de Rijcke, S., & Zeilinger, W. W. 2011, *MNRAS*, 417, 1643
- Labbé, I., Oesch, P. A., Bouwens, R. J., et al. 2013, *ApJ*, 777, L19
- Law, D. R., Yan, R., Bershady, M. A., et al. 2015, *AJ*, 150, 19
- Le Borgne, J.-F., Bruzual, G., Pelló, R., et al. 2003, *A&A*, 402, 433
- Lee, K.-S., Ferguson, H. C., Wiklind, T., et al. 2012, *ApJ*, 752, 66
- Lee, N., Sanders, D. B., Casey, C. M., et al. 2015, *ApJ*, 801, 80
- Lee, S.-K., Ferguson, H. C., Somerville, R. S., Wiklind, T., & Giavalisco, M. 2010, *ApJ*, 725, 1644
- Lehnert, M. D., Di Matteo, P., Haywood, M., & Snaith, O. N. 2014, *ApJ*, 789, L30
- Lehnert, M. D., van Driel, W., Le Tiran, L., Di Matteo, P., & Haywood, M. 2015, *A&A*, 577, A112
- Li, C. & White, S. D. M. 2009, *MNRAS*, 398, 2177
- Lilly, S. J., Carollo, C. M., Pipino, A., Renzini, A., & Peng, Y. 2013, *ApJ*, 772, 119
- Lilly, S. J., Le Fèvre, O., Hammer, F., & Crampton, D. 1996, *ApJ*, 460, L1
- Lofthouse, E. K., Kaviraj, S., Conselice, C. J., Mortlock, A., & Hartley, W. 2017, *MNRAS*, 465, 2895
- López Fernández, R., Cid Fernandes, R., González Delgado, R. M., et al. 2016, *MNRAS*, 458, 184
- López-Sanjuan, C., Cenarro, A. J., Varela, J., et al. 2015, *A&A*, 576, A53
- López-Sanjuan, C., Le Fèvre, O., Ilbert, O., et al. 2012, *A&A*, 548, A7
- Lotz, J. M., Jonsson, P., Cox, T. J., et al. 2011, *ApJ*, 742, 103
- Madau, P. & Dickinson, M. 2014, *ARA&A*, 52, 415
- Madau, P., Pozzetti, L., & Dickinson, M. 1998, *ApJ*, 498, 106
- Magdis, G. E., Elbaz, D., Daddi, E., et al. 2010, *ApJ*, 714, 1740
- Man, A. W. S., Toft, S., Zirm, A. W., Wuyts, S., & van der Wel, A. 2012, *ApJ*, 744, 85
- Marchesini, D., van Dokkum, P. G., Förster Schreiber, N. M., et al. 2009, *ApJ*, 701, 1765
- Martin, D. C., Fanson, J., Schiminovich, D., et al. 2005, *ApJ*, 619, L1
- Martin, G., Kaviraj, S., Devriendt, J. E. G., et al. 2017, *MNRAS*, 472, L50
- Martins, L. P., González Delgado, R. M., Leitherer, C., Cerviño, M., & Hauschildt, P. 2005, *MNRAS*, 358, 49
- McDermid, R. M., Alatalo, K., Blitz, L., et al. 2015, *MNRAS*, 448, 3484
- Minchev, I., Chiappini, C., Martig, M., et al. 2014, *ApJ*, 781, L20
- Morrissey, P., Conrow, T., Barlow, T. A., et al. 2007, *ApJS*, 173, 682
- Moustakas, J., Coil, A. L., Aird, J., et al. 2013, *ApJ*, 767, 50
- Moustakas, L. A. & Metcalf, R. B. 2003, *MNRAS*, 339, 607
- Muzzin, A., Marchesini, D., Stefanon, M., et al. 2013, *ApJ*, 777, 18
- Naab, T. & Ostriker, J. P. 2016, *ArXiv e-prints*
- Neistein, E. & Dekel, A. 2008, *MNRAS*, 388, 1792
- Neistein, E., van den Bosch, F. C., & Dekel, A. 2006, *MNRAS*, 372, 933
- Nelson, D., Pillepich, A., Genel, S., et al. 2015, *Astronomy and Computing*, 13, 12
- Noeske, K. G., Faber, S. M., Weiner, B. J., et al. 2007, *ApJ*, 660, L47
- Ocvirk, P., Pichon, C., Lançon, A., & Thiébaud, E. 2006, *MNRAS*, 365, 74
- Oliver, S., Frost, M., Farrah, D., et al. 2010, *MNRAS*, 405, 2279
- Pannella, M., Carilli, C. L., Daddi, E., et al. 2009, *ApJ*, 698, L116
- Panther, B., Heavens, A. F., & Jimenez, R. 2003, *MNRAS*, 343, 1145
- Panther, B., Jimenez, R., Heavens, A. F., & Charlot, S. 2007, *MNRAS*, 378, 1550
- Panther, B., Jimenez, R., Heavens, A. F., & Charlot, S. 2008, *MNRAS*, 391, 1117
- Peng, Y.-j., Lilly, S. J., Kovač, K., et al. 2010, *ApJ*, 721, 193
- Pérez, E., Cid Fernandes, R., González Delgado, R. M., et al. 2013, *ApJ*, 764, L1
- Pérez-González, P. G., Rieke, G. H., Villar, V., et al. 2008, *ApJ*, 675, 234
- Pozzetti, L., Bolzonella, M., Zucca, E., et al. 2010, *A&A*, 523, A13
- Reddy, N. A. & Steidel, C. C. 2009, *ApJ*, 692, 778
- Renzini, A. & Peng, Y.-j. 2015, *ApJ*, 801, L29
- Rodighiero, G., Vaccari, M., Franceschini, A., et al. 2010, *A&A*, 515, A8
- Rodríguez-Gomez, V., Genel, S., Vogelsberger, M., et al. 2015, *MNRAS*, 449, 49
- Roth, M. M., Kelz, A., Fechner, T., et al. 2005, *PASP*, 117, 620
- Roškar, R., Debattista, V. P., Quinn, T. R., Stinson, G. S., & Wadsley, J. 2008, *ApJ*, 684, L79
- Rudnick, G., Rix, H.-W., Franx, M., et al. 2003, *ApJ*, 599, 847
- Salim, S., Charlot, S., Rich, R. M., et al. 2004, in *Bulletin of the American Astronomical Society*, Vol. 36, American Astronomical Society Meeting Abstracts, 1411
- Salim, S., Rich, R. M., Charlot, S., et al. 2007, *ApJS*, 173, 267
- Sanchez, S. F., Avila-Reese, V., Hernandez-Toledo, H., et al. 2017, *ArXiv e-prints*
- Sánchez, S. F., García-Benito, R., Zibetti, S., et al. 2016, *A&A*, 594, A36
- Sánchez, S. F., Kennicutt, R. C., Gil de Paz, A., et al. 2012, *A&A*, 538, A8
- Sánchez-Blázquez, P., Peletier, R. F., Jiménez-Vicente, J., et al. 2006, *MNRAS*, 371, 703

- Sánchez-Blázquez, P., Rosales-Ortega, F., Diaz, A., & Sánchez, S. F. 2014a, MNRAS, 437, 1534
- Sánchez-Blázquez, P., Rosales-Ortega, F. F., Méndez-Abreu, J., et al. 2014b, A&A, 570, A6
- Sandage, A. 1986, A&A, 161, 89
- Schiminovich, D., Wyder, T. K., Martin, D. C., et al. 2007, ApJS, 173, 315
- Schmidt, M. 1968, ApJ, 151, 393
- Searle, L., Sargent, W. L. W., & Bagnuolo, W. G. 1973, ApJ, 179, 427
- Simha, V., Weinberg, D. H., Conroy, C., et al. 2014, ArXiv e-prints
- Song, M., Finkelstein, S. L., Ashby, M. L. N., et al. 2016, ApJ, 825, 5
- Sparre, M., Hayward, C. C., Springel, V., et al. 2015, MNRAS, 447, 3548
- Speagle, J. S., Steinhardt, C. L., Capak, P. L., & Silverman, J. D. 2014, ApJS, 214, 15
- Stark, D. P., Ellis, R. S., Bunker, A., et al. 2009, ApJ, 697, 1493
- Stark, D. P., Schenker, M. A., Ellis, R., et al. 2013, ApJ, 763, 129
- Stoughton, C., Lupton, R. H., Bernardi, M., et al. 2002, AJ, 123, 485
- Tasca, L. A. M., Le Fèvre, O., Hathi, N. P., et al. 2015, A&A, 581, A54
- Thomas, D., Maraston, C., & Bender, R. 2003, MNRAS, 339, 897
- Tinsley, B. M. 1968, ApJ, 151, 547
- Tinsley, B. M. 1972, A&A, 20, 383
- Toft, S., Gallazzi, A., Zirm, A., et al. 2012, ApJ, 754, 3
- Tojeiro, R., Percival, W. J., Heavens, A. F., & Jimenez, R. 2011, MNRAS, 413, 434
- Tomczak, A. R., Quadri, R. F., Tran, K.-V. H., et al. 2016, ApJ, 817, 118
- Trager, S. C., Faber, S. M., Worthey, G., & González, J. J. 2000, AJ, 119, 1645
- Vazdekis, A., Sánchez-Blázquez, P., Falcón-Barroso, J., et al. 2010, MNRAS, 404, 1639
- Verheijen, M. A. W., Bershady, M. A., Andersen, D. R., et al. 2004, Astronomische Nachrichten, 325, 151
- Walcher, C. J., Wisotzki, L., Bekeraité, S., et al. 2014, A&A, 569, A1
- Walcher, J., Groves, B., Budavári, T., & Dale, D. 2011, Ap&SS, 331, 1
- Weinmann, S. M., Neistein, E., & Dekel, A. 2011, MNRAS, 417, 2737
- Whitaker, K. E., van Dokkum, P. G., Brammer, G., & Franx, M. 2012, ApJ, 754, L29
- Williams, R. J., Quadri, R. F., & Franx, M. 2011, ApJ, 738, L25
- Worthey, G. 1994, ApJS, 95, 107
- Wuyts, S., Förster Schreiber, N. M., van der Wel, A., et al. 2011, ApJ, 742, 96
- Wyder, T. K., Martin, D. C., Schiminovich, D., et al. 2007, ApJS, 173, 293
- Yabe, K., Ohta, K., Iwata, I., et al. 2009, ApJ, 693, 507
- Zibetti, S., Gallazzi, A. R., Ascasibar, Y., et al. 2017, ArXiv e-prints



## Appendix A: Comparing results from parametric and non-parametric SFHs

In this appendix we compare the SFHs obtained with the delayed- $\tau$  model with those obtained with other models, parametric and non-parametric (the `STARLIGHT` code). We express the SFH by the mass fraction,  $m(t)$ , defined for each galaxy as the ratio of the mass formed in each epoch to the total mass of the galaxy today. We also derive the mass growth curve (see e.g. Pérez et al. 2013; García-Benito et al. 2017), which provides useful information about how the mass is assembled in a galaxy as a whole and in different regions. From these curves, we compare the epoch at which galaxies assembled 80% of their current mass,  $t_{80}$ . Finally, we estimate  $\rho_{\text{SFR}}$ ,  $\rho_*$ , and sSFR at different redshifts, and we compare the results from the different models with those from surveys at different redshifts. The goal of this Appendix is to show that delayed- $\tau$  model is the most simple, meaningful, and representative parameterization of the SFHs.

### Appendix A.1: delayed- $\tau$ vs non-parametric SFH with `STARLIGHT`

Our previous analysis obtained with `STARLIGHT` for the CALIFA sample presented in González Delgado et al. (2017) was done by fitting only the CALIFA spectra, using composite stellar population models built with SSPs by Vazdekis et al. (2010) and González Delgado et al. (2005) assuming a Salpeter IMF. In terms of  $m(t)$ , we obtain that the highest mass fractions invariably occur at the earliest times, and subsequent star formation varies systematically with  $M_*$  and morphology, with the low  $M_*$  and also the later spiral galaxies forming stars over more extended periods of time, while high  $M_*$  and early type galaxies exhibit the fastest decline in  $m(t)$ .

In order to be consistent with the data, here we use `STARLIGHT` but now fitting the GALEX (FUV, NUV) photometry and the full CALIFA spectra.<sup>8</sup> The fits are done with the new version of `STARLIGHT` by López Fernández et al. (2016) in combination with the same collection of SSPs by Charlot & Bruzual (2007) used with M1. We also assume a Chabrier IMF.

To quantify the differences between the `STARLIGHT` and the delayed- $\tau$  model we have discretized  $m(t)$  in a few relevant age ranges. Fig. A.1 presents the results for four age ranges:  $t \leq 1$  Gyr (blue),  $1 < t \leq 4$  Gyr (green),  $4 < t \leq 9$  Gyr (yellow), and  $t \geq 9$  Gyr (red). Each panel shows three bar charts corresponding to the spatial regions:  $R < 0.5$  HLR (left), the whole galaxy (middle), and the outer regions  $1 < R < 2$  HLR. The results from the delayed- $\tau$  model (M1) and `STARLIGHT` (ST) are presented in the middle and left columns.

As with ST, most of the stellar mass in M1 is formed very early on and with very little mass in stars younger than 1 Gyr. Notice that the major differences occur in a similar way for all the morphological types. Thus, we can conclude that with ST non-parametric SFH we derive a larger fraction of old stellar populations ( $t > 9$  Gyr and/or  $4 < t < 9$  Gyr) and less intermediate and young components ( $1 < t < 4$  Gyr and/or  $t < 1$  Gyr). To comment in more detail these differences, we discuss the results for the inner regions:

- $m(t \leq 1)$ : this mass fraction increases from E to Sd, although the fraction is lower in the inner regions than in the outer ones. With ST,  $m(t \leq 1) \leq 1\%$  in Sbc and earlier types, increasing to  $m(t \leq 1) \sim 6\%$  and  $9\%$  for Sc and Sd, respec-

<sup>8</sup> Instead of GALEX and SDSS photometry and the spectroscopic indexes,  $D_n4000$ ,  $H\beta$ , and  $[\text{FeMg}]'$  used in M1.

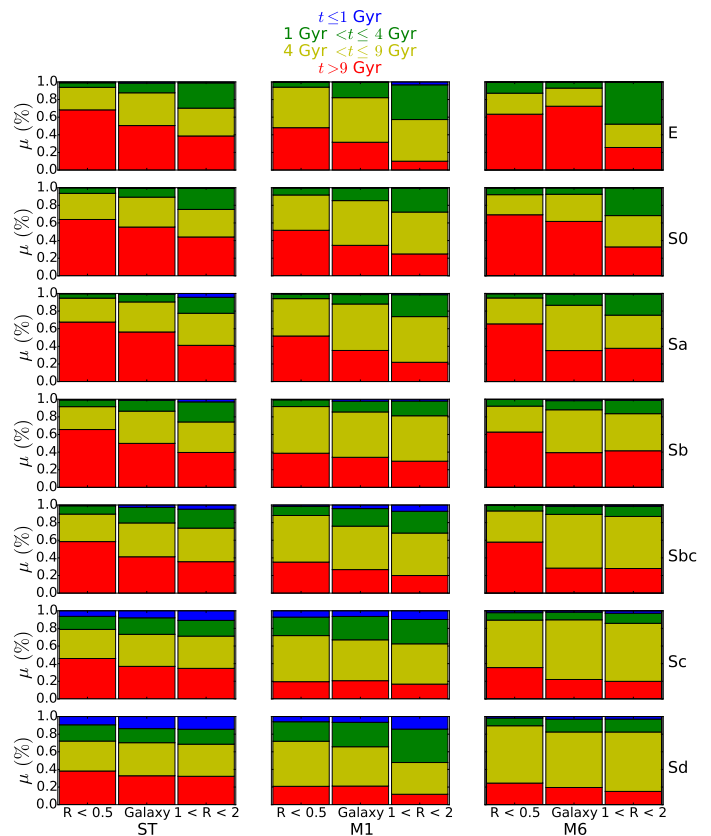


**Fig. A.1.** Results of mass fraction  $m(t)$  grouped in four different age ranges (color coded as indicated on the top) from `STARLIGHT` (ST, left), the delayed- $\tau$  model (M1, middle), and a two-exponential model (M6, right).

tively. Using M1,  $m(t \leq 1) \leq 2\%$  in Sbc and earlier types increasing to  $m(t \leq 1) \sim 7\%$  and  $6\%$  for Sc and Sd galaxies, respectively.

- $m(1 < t \leq 4)$ : on average, we obtain lower mass fractions of this component in the inner than in the outer regions for all the Hubble types and all the models. Using ST and M1, the mass fraction of this component increases from early to late type galaxies. For E galaxies,  $m(1 < t \leq 4) \sim 5\%$  and  $6\%$ , for ST and M1, respectively. On the other hand, for Sd galaxies,  $m(1 < t \leq 4) \sim 19\%$  and  $22\%$ , respectively.
- $m(4 < t \leq 9)$ : with ST and M1, we obtain similar mass fractions of this component for all the Hubble types. With ST,  $20\% \leq m(4 < t \leq 9) \leq 30\%$ . For M1, we obtain  $3\% \leq m(4 < t \leq 9) \leq 46\%$  for E, S0, and Sa galaxies;  $m(4 < t \leq 9) \sim 53\%$  for Sb, Sbc, and Sc; and  $m(4 < t \leq 9) \sim 52\%$  for Sd galaxies.
- $m(t > 9)$ : for all the models the old component decreases from E to Sd galaxies and is larger in the inner region. For E galaxies,  $m(t > 9) \sim 74\%$  and  $48\%$ , for ST and M1, respectively. For Sd galaxies,  $m(t > 9) \sim 42\%$  and  $21\%$ , respectively.

Other interesting results come from the comparison of the epoch at which galaxies assemble 80% of their mass,  $t_{80}$ . From our previous analysis with `STARLIGHT`, Pérez et al. (2013) and García-Benito et al. (2017) found that the most massive galaxies assembled their mass earlier than the low mass galaxies, a signature of downsizing. We have also obtained that  $t_{80}$  for the inner regions is higher than for the outer regions, suggesting that galaxies assemble their mass inside-out.

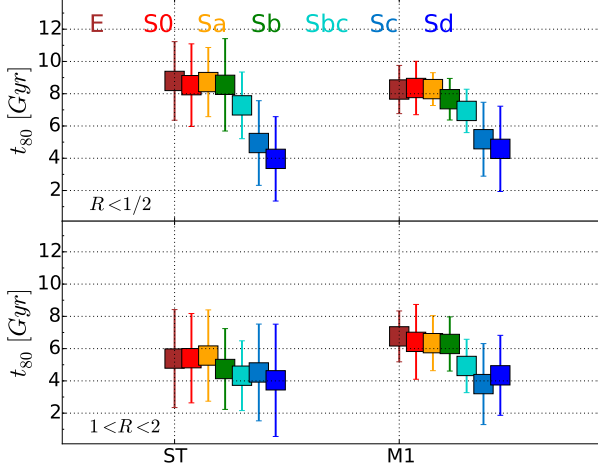


**Fig. A.2.** Lookback time at which galaxies assemble 80% of their mass,  $t_{80}$ , from STARLIGHT and from M1, corresponding to the inner  $R < 0.5$  HLR and outer regions  $1 < R < 2$  HLR.

Figure A.2 compares the results from M1 and ST for  $t_{80}$  in the inner and outer regions. They are:

- Inner regions: 1) M1,  $t_{80}$  decreases with Hubble type, with E, S0, and Sa having similar values,  $t_{80} \sim 9 - 8$  Gyr, while  $t_{80} \sim 5$  Gyr for Sc and Sd. 2) The results with ST are very similar,  $t_{80}$  decreasing from early to late types. For Sb and earlier types,  $t_{80} \sim 8 - 9$  Gyr,  $t_{80} \sim 5$  Gyr for Sc, and  $t_{80} \sim 4$  Gyr for Sd, slightly lower than with M1.
- Outer regions: 1) M1,  $t_{80}$  decreases with the morphology, lower for later types. The values for the outer regions are lower than for the inner ones for all types. For Sb and earlier types  $t_{80} \sim 6 - 7$  Gyr, and for Sd galaxies  $t_{80} \sim 4$  Gyr. 2) With ST,  $t_{80}$  decreases similarly with Hubble type, from  $t_{80} \sim 5 - 6$  Gyr for Sa and later types to  $t_{80} \sim 4$  Gyr for Sd.

#### Appendix A.2: delayed- $\tau$ vs other parametric SFHs

Other parametric SFHs have been used to fit the observational constrains. They are of two types:

a) One single function, as in the  $\tau$  model:

- A  $\tau$  model (M2):

$$\psi(t) = \psi_0 e^{-(t_0-t)/\tau}$$

- Sandage model (Sandage 1986) (M3):

$$\psi(t) = \frac{A}{\tau^2} (t_0 - t) e^{-(t_0-t)^2/2\tau^2}$$

- Linearly-rising (M4):

$$\psi(t) = \psi_0 - \frac{d\psi}{dt} (t_0 - t)$$

- Power rising (M5):

$$\psi(t) = \psi_0 (t_0 - t)^\alpha$$

b) A combination of two functions:

$$\Delta = \frac{\text{Synthetic} - \text{Observed}}{\text{Error}}$$

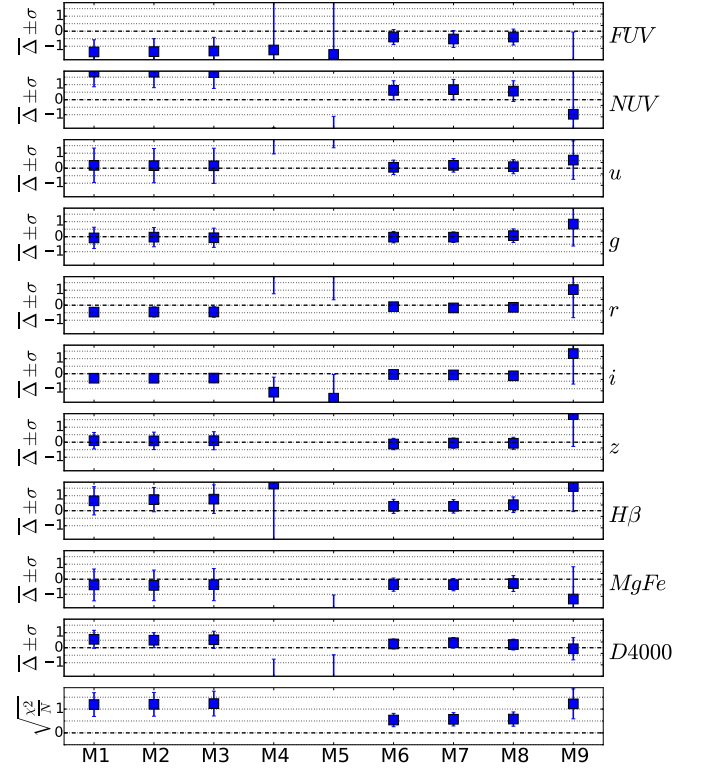


**Fig. A.3.** Quality of the fits using the different models. Each panel shows  $\Delta \pm \sigma$  for each of the observables.  $\Delta$  is the average of the difference between the synthetic and the observable quantity divided by the error. The bottom panel, however, shows the reduced  $\chi^2$ .

- Two exponentials (M6):

$$\psi_{old}(t) = \psi_0 e^{-(t_0^{old}-t)/\tau^{old}}$$

$$\psi_{young}(t) = \psi_0 e^{-(t_0^{young}-t)/\tau^{young}}$$

- Two exponentials, with old component fixed (M7):

$$\psi_{old}(t) = \psi_0 e^{-(14\text{Gyr}-t)/\tau^{old}}$$

$$\psi_{young}(t) = \psi_0 e^{-(t_0^{young}-t)/\tau^{young}}$$

- An exponential plus a Sandage component (M8):

$$\psi_{old}(t) = \psi_0 e^{-(t_0^{old}-t)/\tau^{old}}$$

$$\psi_{young}(t) = \frac{A}{[\tau^{young}]^2} (t_0^{young} - t) e^{-(t_0^{young}-t)^2/2[\tau^{young}]^2}$$

- Constant SFR plus an exponential declining (M9):

$$\psi_{old}(t) = \psi_0$$

$$\psi_{young}(t) = \psi_0 e^{-(t_0-t)/\tau}$$

Figure A.3 shows the quality of the fits; we conclude: a) M2 and M3 provide similar quality in the fits that M1; b) M4 and M5 give very poor fits; c) the quality of the fits with M6, M7, and M8 are somewhat better than with M1; d) M9 provides fits

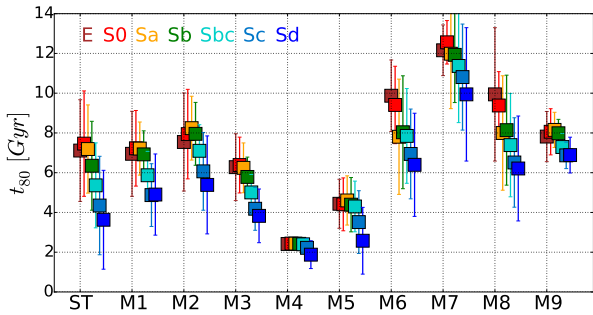


**Fig. A.4.** Lookback time at which galaxies assemble 80% of their mass,  $t_{80}$ , from the different parametric models and STARLIGHT. The average values are color coded as a function of morphology.

of similar quality to M1. Although M1 is not the model with the lowest  $\chi^2$ , the results related with the star formation history of galaxies and stellar population properties are better than with the other models, as explained below; so we use M1 as the reference model.

Figure A.1 shows a detailed comparison between M6, M1, and STARLIGHT. Table A.1 lists the results for all the models.

To show further differences and similarities between the parametric models and STARLIGHT, Fig. A.4 shows  $t_{80}$  calculated for the whole galaxy ( $R < 2$  HLR). The results are averaged by Hubble type:

- Except for M4, the parametric and non-parametric models show that  $t_{80}$  decreases with Hubble type. This is a manifestation of the downsizing scenario since in our sample, on average, the galaxy mass scales with Hubble type. Notice, however, that the range of variation from E to Sd is smaller with M5 and M9.
- With STARLIGHT,  $t_{80} \sim 7$  Gyr for Sa and earlier types and decreases for later types, down to  $t_{80} \sim 3.5$  Gyr for Sd. Results with M1 are very similar to STARLIGHT for Sa and earlier types, with  $t_{80} \sim 7$  Gyr; but for later types, Sd, STARLIGHT gives smaller  $t_{80}$  than M1.
- For M2,  $t_{80} \sim 8$  Gyr for S0 and Sb, and larger for Sa. For E,  $t_{80} \sim 7.5$  Gyr and smaller values are obtained for later spirals, with  $t_{80} \sim 5.5$  Gyr for Sd.
- M3 gives smaller values than M1. For Sa and earlier types  $t_{80} \sim 6 - 7$  Gyr,  $t_{80} \sim 6$  Gyr for Sb galaxies, and  $t_{80} \sim 4$  Gyr for Sc and Sd.
- Results with M6 and M8 are very similar. In both cases,  $t_{80}$  decreases from 10 Gyr in E galaxies to 6-7 Gyr for Sc and Sd.
- With M7,  $t_{80}$  is larger for all the Hubble types. For Sd  $t_{80} \sim 10$  Gyr, which is the value obtained for E galaxies with M6 and M8. For E and S0 galaxies,  $t_{80} \sim 12-13$  Gyr.
- The range of variation of  $t_{80}$  with M9 is lower than with the other models. For Sb and earlier types,  $t_{80} \sim 8$  Gyr, while for Sc and Sd  $t_{80} \sim 7$  Gyr.

### Appendix A.3: Fossil cosmology vs galaxy surveys: $\rho_{\text{SFR}}$ , sSFR, and $\rho_*$

Finally we compare the results from the different models with fossil cosmology with respect to galaxy surveys, calculating  $\rho_{\text{SFR}}$ , sSFR, and  $\rho_*$  as a function of redshift. In Section 5 we compared these properties for model M1 with results from

galaxy surveys from the literature. Here we extend the comparisons to all the parametric models presented in this Appendix. From Fig. A.5, we conclude:

- **M2**:  $\rho_{\text{SFR}}$  increases with redshift, and it does not show a maximum (or plateau) at  $z \sim 2$  as the cosmological galaxy surveys do.  $\rho_*$  increases with time more rapidly than any other single parametric SFH, and the galaxy surveys. sSFR( $t$ ) for  $z > 0.5$  are below the lower envelope of points from the cosmological galaxy surveys.
- **M3**:  $\rho_{\text{SFR}}$  has the maximum at intermediate redshift  $z \sim 1$ . The evolution of sSFR( $t$ ) is very similar to model M1 and the individual measurements from galaxy surveys. However,  $\rho_*$  increases more slowly than M1 and galaxy surveys, although it gets a similar value than M1 at  $z = 0$ .
- **M4 and M5**: they give very unrealistic results for the SFH of nearby galaxies, and are not able to fit well the observational constrains (see Fig. A.3). Moreover,  $\rho_{\text{SFR}}$ ,  $\rho_*$ , and sSFR( $t$ ) do not match the results from galaxy surveys. At  $z = 0$ , with these models  $\rho_{\text{SFR}}$  is significantly higher than in cosmological galaxy surveys, and at  $z \geq 1$  significantly lower. sSFR( $t$ ) evolves with time more smoothly than galaxy surveys do. M4 gives a cosmic evolution of  $\rho_*$  that does not match at all the points from galaxy surveys; and M5 gives values of  $\rho_*$  at intermediate redshift that are not in agreement with results from galaxy surveys.
- **M6 and M8**:  $\rho_{\text{SFR}}$ , sSFR( $t$ ), and  $\rho_*$  are similar to galaxy surveys, except that sSFR( $t$ ) at  $z \geq 2$  is lower than the values of the literature. These models not provide  $m(t)$  that is very different to that obtained by Madau & Dickinson (2014) (see Fig. 9).
- **M7**: the fraction in stars older than 9 Gyr is significantly higher than for the other models, and thus the galaxies grow their mass very rapidly and very early on. As a consequence, the fraction of stellar mass in components of intermediate ages are low. Thus, although at  $z = 0$  and  $z \sim 4$ ,  $\rho_{\text{SFR}}$  is similar to cosmological galaxy surveys, its evolution is quite different to the results from these works, since a minimum happens at intermediate redshifts. Similarly, sSFR( $t$ ) for  $z > 0.5$  is quite low in comparison with galaxy surveys. In contrast,  $\rho_*$  does not evolve with time, being almost constant since  $z \leq 5$ .
- **M9**: the evolution of  $\rho_{\text{SFR}}$  up to  $z = 2$  is similar to galaxy surveys, but it does not show a change of slope at  $z > 2$  and it continues increasing with redshift. In absolute values  $\rho_{\text{SFR}} \sim 0.2 - 0.3$  dex below the Madau & Dickinson (2014) curve. sSFR( $t$ ) is significantly below the Elbaz et al. (2011) curve, this is also a consequence of the rapid growth of  $\rho_*$ .

		E	S0	Sa	Sb	Sbc	Sc	Sd
ST	$m_{t<1\text{ Gyr}}$	$1 \pm 3$	$1 \pm 1$	$1 \pm 1$	$1 \pm 1$	$2 \pm 2$	$7 \pm 14$	$13 \pm 18$
	$m_{1<t<4\text{ Gyr}}$	$11 \pm 11$	$10 \pm 14$	$9 \pm 8$	$12 \pm 10$	$18 \pm 14$	$19 \pm 16$	$16 \pm 14$
	$m_{4<t<9\text{ Gyr}}$	$30 \pm 21$	$28 \pm 18$	$29 \pm 16$	$32 \pm 17$	$35 \pm 12$	$33 \pm 15$	$34 \pm 15$
	$m_{t>9\text{ Gyr}}$	$58 \pm 25$	$61 \pm 23$	$61 \pm 20$	$54 \pm 22$	$45 \pm 19$	$40 \pm 20$	$36 \pm 19$
M1	$m_{t<1\text{ Gyr}}$	$1 \pm 1$	$1 \pm 1$	$1 \pm 1$	$2 \pm 2$	$4 \pm 2$	$6 \pm 3$	$7 \pm 4$
	$m_{1<t<4\text{ Gyr}}$	$17 \pm 31$	$14 \pm 27$	$10 \pm 13$	$12 \pm 11$	$20 \pm 14$	$26 \pm 17$	$28 \pm 21$
	$m_{4<t<9\text{ Gyr}}$	$51 \pm 30$	$51 \pm 28$	$53 \pm 20$	$51 \pm 16$	$49 \pm 10$	$46 \pm 10$	$45 \pm 15$
	$m_{t>9\text{ Gyr}}$	$32 \pm 28$	$35 \pm 27$	$36 \pm 21$	$34 \pm 17$	$27 \pm 11$	$21 \pm 12$	$21 \pm 17$
M2	$m_{t<1\text{ Gyr}}$	$1 \pm 1$	$1 \pm 1$	$1 \pm 1$	$2 \pm 2$	$3 \pm 1$	$8 \pm 18$	$6 \pm 4$
	$m_{1<t<4\text{ Gyr}}$	$16 \pm 20$	$11 \pm 26$	$9 \pm 14$	$10 \pm 12$	$16 \pm 16$	$20 \pm 19$	$30 \pm 27$
	$m_{4<t<9\text{ Gyr}}$	$47 \pm 26$	$44 \pm 24$	$39 \pm 23$	$37 \pm 16$	$37 \pm 10$	$37 \pm 13$	$39 \pm 23$
	$m_{t>9\text{ Gyr}}$	$37 \pm 27$	$44 \pm 25$	$51 \pm 26$	$51 \pm 20$	$48 \pm 14$	$35 \pm 17$	$25 \pm 24$
M3	$m_{t<1\text{ Gyr}}$	$1 \pm 1$	$1 \pm 1$	$1 \pm 1$	$2 \pm 2$	$5 \pm 2$	$7 \pm 3$	$8 \pm 4$
	$m_{1<t<4\text{ Gyr}}$	$18 \pm 28$	$15 \pm 23$	$14 \pm 11$	$18 \pm 15$	$24 \pm 12$	$29 \pm 11$	$33 \pm 17$
	$m_{4<t<9\text{ Gyr}}$	$61 \pm 27$	$60 \pm 20$	$62 \pm 15$	$59 \pm 14$	$54 \pm 9$	$50 \pm 8$	$46 \pm 14$
	$m_{t>9\text{ Gyr}}$	$21 \pm 20$	$24 \pm 16$	$23 \pm 16$	$21 \pm 9$	$17 \pm 6$	$14 \pm 6$	$12 \pm 7$
M4	$m_{t<1\text{ Gyr}}$	$15 \pm 1$	$15 \pm 1$	$15 \pm 1$	$15 \pm 1$	$15 \pm 2$	$18 \pm 12$	$24 \pm 19$
	$m_{1<t<4\text{ Gyr}}$	$38 \pm 2$	$38 \pm 1$	$38 \pm 1$	$38 \pm 1$	$38 \pm 3$	$40 \pm 8$	$42 \pm 12$
	$m_{4<t<9\text{ Gyr}}$	$38 \pm 2$	$38 \pm 1$	$38 \pm 1$	$38 \pm 1$	$38 \pm 3$	$35 \pm 9$	$29 \pm 14$
	$m_{t>9\text{ Gyr}}$	$9 \pm 1$	$9 \pm 1$	$9 \pm 1$	$9 \pm 1$	$9 \pm 1$	$7 \pm 3$	$5 \pm 4$
M5	$m_{t<1\text{ Gyr}}$	$10 \pm 5$	$14 \pm 20$	$13 \pm 18$	$14 \pm 21$	$11 \pm 12$	$16 \pm 18$	$25 \pm 24$
	$m_{1<t<4\text{ Gyr}}$	$29 \pm 11$	$25 \pm 7$	$25 \pm 8$	$25 \pm 8$	$28 \pm 10$	$32 \pm 12$	$379 \pm 16$
	$m_{4<t<9\text{ Gyr}}$	$39 \pm 10$	$38 \pm 11$	$38 \pm 10$	$38 \pm 10$	$39 \pm 10$	$36 \pm 11$	$29 \pm 16$
	$m_{t>9\text{ Gyr}}$	$22 \pm 11$	$23 \pm 10$	$25 \pm 8$	$23 \pm 10$	$21 \pm 11$	$15 \pm 12$	$9 \pm 11$
M6	$m_{t<1\text{ Gyr}}$	$1 \pm 1$	$1 \pm 1$	$1 \pm 4$	$2 \pm 5$	$2 \pm 3$	$2 \pm 3$	$3 \pm 7$
	$m_{1<t<4\text{ Gyr}}$	$11 \pm 17$	$9 \pm 12$	$14 \pm 22$	$11 \pm 21$	$8 \pm 21$	$8 \pm 20$	$14 \pm 23$
	$m_{4<t<9\text{ Gyr}}$	$20 \pm 21$	$35 \pm 26$	$49 \pm 20$	$47 \pm 20$	$62 \pm 21$	$71 \pm 25$	$67 \pm 26$
	$m_{t>9\text{ Gyr}}$	$69 \pm 30$	$55 \pm 28$	$36 \pm 21$	$40 \pm 21$	$28 \pm 20$	$19 \pm 24$	$16 \pm 22$
M7	$m_{t<1\text{ Gyr}}$	$1 \pm 1$	$1 \pm 1$	$1 \pm 2$	$1 \pm 4$	$1 \pm 3$	$2 \pm 4$	$3 \pm 8$
	$m_{1<t<4\text{ Gyr}}$	$8 \pm 8$	$5 \pm 9$	$12 \pm 20$	$8 \pm 15$	$7 \pm 16$	$6 \pm 14$	$8 \pm 16$
	$m_{4<t<9\text{ Gyr}}$	$5 \pm 7$	$4 \pm 6$	$2 \pm 4$	$4 \pm 6$	$6 \pm 7$	$10 \pm 10$	$12 \pm 10$
	$m_{t>9\text{ Gyr}}$	$86 \pm 11$	$90 \pm 10$	$85 \pm 21$	$87 \pm 19$	$86 \pm 20$	$82 \pm 21$	$76 \pm 24$
M8	$m_{t<1\text{ Gyr}}$	$1 \pm 1$	$2 \pm 6$	$1 \pm 3$	$1 \pm 3$	$1 \pm 2$	$2 \pm 3$	$3 \pm 7$
	$m_{1<t<4\text{ Gyr}}$	$7 \pm 8$	$3 \pm 7$	$13 \pm 25$	$9 \pm 20$	$9 \pm 22$	$12 \pm 25$	$20 \pm 22$
	$m_{4<t<9\text{ Gyr}}$	$39 \pm 25$	$36 \pm 27$	$48 \pm 29$	$50 \pm 23$	$65 \pm 30$	$70 \pm 25$	$60 \pm 28$
	$m_{t>9\text{ Gyr}}$	$53 \pm 26$	$59 \pm 28$	$38 \pm 23$	$39 \pm 25$	$25 \pm 29$	$16 \pm 21$	$17 \pm 22$
M9	$m_{t<1\text{ Gyr}}$	$1 \pm 1$	$1 \pm 1$	$1 \pm 1$	$2 \pm 1$	$3 \pm 1$	$4 \pm 1$	$4 \pm 2$
	$m_{1<t<4\text{ Gyr}}$	$9 \pm 8$	$8 \pm 7$	$8 \pm 5$	$9 \pm 4$	$14 \pm 4$	$16 \pm 4$	$16 \pm 5$
	$m_{4<t<9\text{ Gyr}}$	$40 \pm 7$	$39 \pm 7$	$39 \pm 5$	$39 \pm 4$	$40 \pm 1$	$40 \pm 1$	$40 \pm 2$
	$m_{t>9\text{ Gyr}}$	$50 \pm 12$	$52 \pm 11$	$52 \pm 9$	$50 \pm 7$	$43 \pm 6$	$40 \pm 5$	$40 \pm 7$

**Table A.1.** Average mass fraction, corresponding to the whole galaxy, due to stars in different age ranges as a function of Hubble type, obtained with STARLIGHT and with the parametric models.

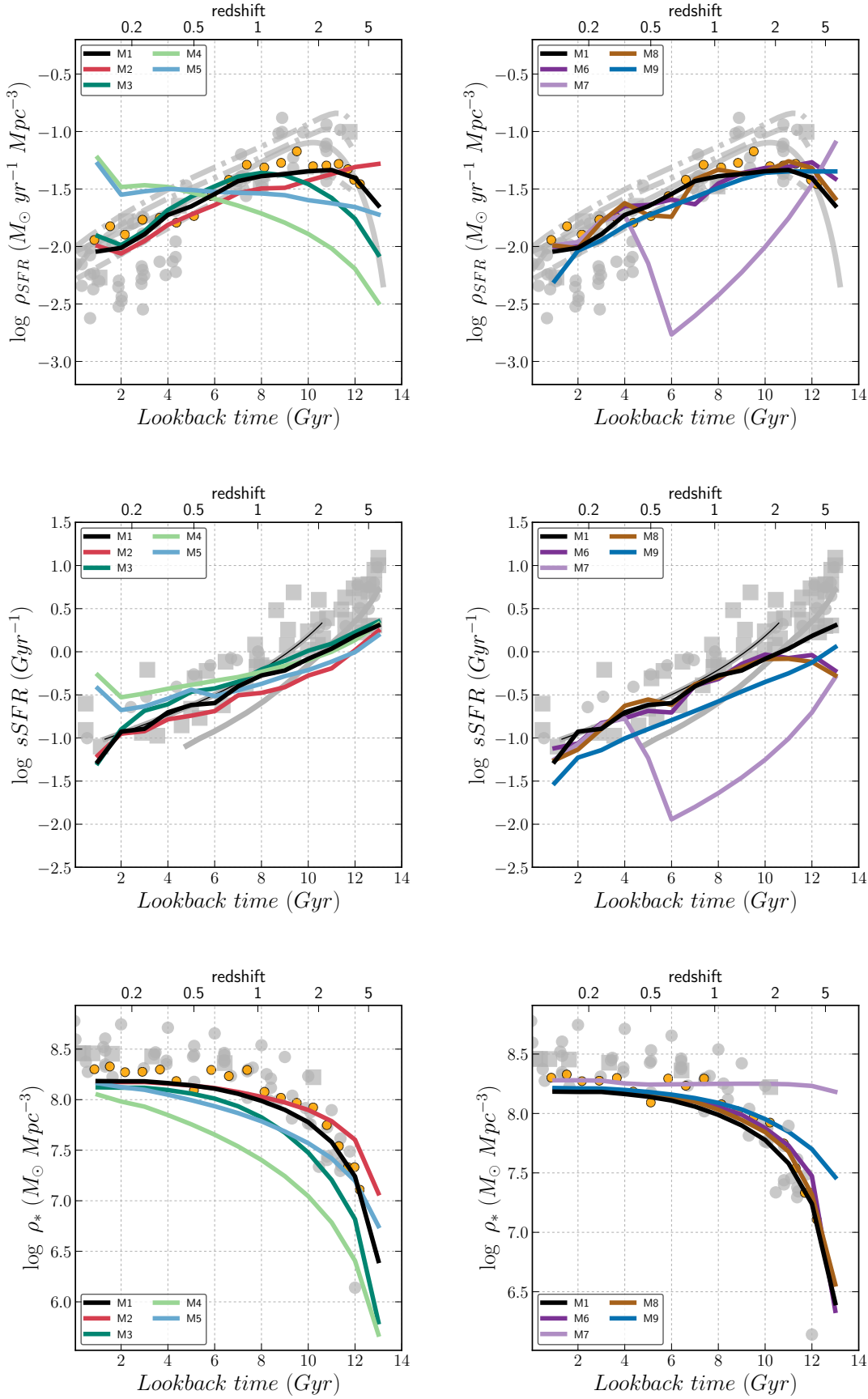


**Fig. A.5.** Cosmic evolution of SFR ( $\rho_{\text{SFR}}$ , upper panels), sSFR (middle panels), and stellar mass ( $\rho_*$ , bottom panels), for one single parametric SFH (left panels) and a combination of two parametric SFH (right panels). The reference delayed- $\tau$  model (M1, black line) is plotted in all the panels. Gray and yellow points, and gray curves are taken from the literature as explained in the text and in the captions of Fig. 6, Fig. 7, and Fig. 8.